Title

Field-scale estimation of soil properties from spectral induced polarization tomography

Authors

Revil, A
Schmutz, M
Abdulsamad, F
et al.

Publication Date

2021-12-01

DOI

10.1016/j.geoderma.2021.115380

Peer reviewed

Field-scale Estimation of Soil Properties from Spectral Induced Polarization Tomography

A. Revil[1], M. Schmutz[2], F. Abdulsamad[3], A. Balde[2,4], C. Beck [5],

A. Ghorbani[6], and S. S. Hubbard[4]

(1) Univ. Grenoble Alpes, Univ. Savoie Mont-Blanc, CNRS, UMR CNRS 5204, EDYTEM, 73370 Le Bourget du Lac, France
(2) Bordeaux INP – Université Bordeaux Montaigne, EA4592 Géoressources et Environnement, Talence, France
(3) Univ. Savoie Mont-Blanc, CNRS, UMR CNRS 5271, LOCIE, 73370 Le Bourget du Lac, France
(4) Lawrence Berkeley National Laboratory, Earth & Environmental Sciences, CA 94720, USA
(5) Université Grenoble Alpes, CNRS, IRD, IFSTTAR, ISTerre, 38000 Grenoble, France
(6) Yazd University, Department of Mining and Metallurgical Engineering, Yazd, Iran.

Corresponding author: André Revil andre.revil@univ-smb.fr

Emails: myriam.schmutz@ipb.fr; andre.revil@univ-smb.fr; feras.abdulsamad@univ-smb.fr; abdoulaye.balde@ipb.fr; sshubbard@lbl.gov; christian.beck@univ-smb.fr; ah.ghorbani@yahoo.fr

Highlights: (1) Laboratory investigations were used to refine a petrophysical model that links induced polarization properties to soil characteristics. (2) We image the spatial distribution of soil water content, CEC, mean grain size and permeability i. (3) Induced polarization is now mature enough to be used in agriculture and to study the critical zone.

Intended for publication in *GEODERMA*

Abstract. Estimates of soil properties such as Cation Exchange Capacity (CEC), water content, grain size characteristics, and permeability are important in geotechnical engineering, water resources, and agriculture. We develop a non-intrusive approach to estimate these properties in the field using spectral induced polarization (SIP) tomography. This geophysical method provides information about the frequency dependence of the complex electrical conductivity of porous media. Using 18 soil samples collected from a Bordeaux vineyard, we first conducted a laboratory study using SIP over the frequency range 10 mHz-45 kHz. The laboratory data were used to confirm the accuracy of a recently developed dynamic Stern layer petrophysical model. The results are consistent with published values from previous works using soils. A comparison was made by comparing the field complex conductivity spectra and the experimental data at two locations where core samples were obtained. The model was then used in concert with field data to image the spatial distribution of CEC, water content, permeability, and mean grain size along a vineyard transect. For clay and sandy textures found in the field, measured and estimated CEC agree rather well (from 6 to 40% discrepancy). Our approach provides an efficient way to estimate important soil properties in a non-invasive manner, in high resolution, and over field-relevant scales of the critical zone of the Earth.

Keywords: Induced polarization; chargeability, soil; grain size, cation exchange capacity, water content, tomography, critical zone.

1. Introduction

Soils are an essential component for supporting life on Earth. Currently, climate change and land-use change (including mechanical, chemical, and biological disturbances) are significantly reshaping soil systems (e.g., Acclimaterra Report, 2018). One of the main challenges of the coming decades is to combine protection of this finite soil resource (IPCC Special Report on Climate Change and Land, 2019) and its use in relation with the important context of growth of the world population. Optimal protection and management of soil properties for soil conservation (Dumanski and Peiretti, 2013), geotechnical engineering of the critical zone (Arthur, 2017), water resources (Arya et al., 1981; Ghanbarian et al., 2017), and agriculture (Sainju and Singh, 1997; Oliver et al., 2013) require accurate information about soil properties over field-relevant scales including soil grain size, permeability, cation exchange capacity (CEC), and water content.

Soil particle size distribution is an important soil property as it controls soil texture (e.g., Yolcubal et al., 2004), which is in turm essential regarding soil management. The connection between soil texture and plant competition is well-known in agricultural/viticultural soil management (e.g., van Leeuwen, 2010; Oliver et al. 2013) as well as in ecology of species management (e.g., Pennington et al., 2017; Eckhart et al., 2017). The clay, silt, sand or gravel fraction of soil texture also influence the permeability, a key parameter needed for groundwater flow and transport modeling (Lambe, 1955; Ikard et al., 2014, Hubbard, 2010). Granulometry can be estimated in the laboratory through several methods including sieving/sedimentation approaches. For instance, the French official standard NF X 31-107 involves five particle size classes defining soils categories (clay, silt, fine sand, coarse sand, coarse elements). More advanced methods include laser measurements (NF ISO 13320-1) combined with X-ray methods (i.e., Cnudde and Boone, 2013). Laser

granulometry is a characterization technique based on light diffraction. The laser granulometry allows a continuous grain size distribution between 0.63 and 2000 microns (10 values per decade), relative to sieving/sedimentation method.

Cation exchange capacity (CEC) is an important soil physico-chemical property. It represents the total capacity of soils to retain cations on soil particles at a given soil pH. CEC is mainly related to the content and type of clay and organic matter (Parfitt et al., 1995). It influences nutrient availability and characterize the reaction of soils to fertilizers (Hazleton and Murphy 2007). Water content can be locally determined with different probes such as neutron probes, capacitive sensors, and Time Domain Reflectometry (TDR) (e.g., Gardner, 1986, Topp, 2003). 'While soil sampling for water content determination is precise, it is destructive, time consuming, and often expensive to carry out using the sampling density required to capture natural soil variability (e.g., Gebbers and Adamchuk, 2010).

In recent decades, geophysical methods have been increasingly used for estimating soil texture for environmental and agricultural purposes (e.g., Rubin and Hubbard, 2005; Muzzamal et al., 2018). A variety of non-intrusive methods have also been increasingly used to characterize soil moisture, e.g., Ground Penetrating Radar (GPR) (e.g., Huisman et al., 2003), electromagnetic induction mapping (EIM) of resistivity (e.g., Altdorff et al., 2017; Zare et al., 2020), galvanometric electrical resistivity tomography (ERT, e.g., Friedman, 2005; Shah and Singh, 2005; Brunet et al., 2010), and nuclear magnetic resonance (NMR, Legchenko et al., 2002). Petersen et al. (2005) and André et al. (2012) demonstrated the relevance of geoelectrical methods for the characterization of the distribution of the different soil types, their moisture and CEC (Grote et al., 2010; Li et al., 2018; Martinez et al., 2018; Zare et al., 2020; Zhao, et al., 2020a, b).

Each of these geophysical methods has however intrinsic limitations. For instance GPR cannot be used in presence of conductive materials such as clayey soils. In order to reduce these intrinsic limitations, a combination of methods between geophysical and hard data can represent an efficient approach (e.g., Robinet et al., 2018). While ERT has been widely used to estimate field-scale soil moisture, it is important to recognize that the assumptions used in published works may limit their applications. Electrical conductivity depends on two contributions, bulk and surface conductivities, both characterized by distinct dependence on the water content (Vinegar and Waxman, 1984, Revil et al., 1998). Surface conductivity has been often neglected without justification.

Here, we explore the value of Spectral Induced Polarization (SIP) method for estimating soil properties allowing to reinterpret field conductivity data without the need to neglect surface conductivity. With SIP, both electrical conductivity and (low-frequency) polarization are investigated over a range of frequencies. Polarization refers here to the reversible storage of electrical charges in a soil submitted to an applied electrical current. By low-frequency polarization, we mean polarization mechanisms occurring in the frequency range ~1 mHz-10 kHz.

The polarization mechanisms are operating at the grain or pore scales and are associated with the electrical double layer coating the grains (see Revil et al., 2017a, for soils). The existence of such polarization mechanisms is responsible for a phase lag between the electrical current and the electrical field (Olhoeft, 1981). These polarization mechanisms are different in nature from the dielectric polarization involved at higher frequencies (> 1 MHz) and their study was initially pioneered in the realm of colloidal chemistry (e.g., Dukhin and Shilov, 1974; Fixman, 1980).

Due to several recent key advances, the time has come to explore the value of SIP tomography for field-scale estimation of soil physiochemical properties in soil sciences. One of these developments is related to the existence of precise laboratory and field equipment. In SIP, in addition to measure an amplitude (resistance or conductance), we measure the phase lag between the current and the voltage. Accurate measurements of small phase angles below 1 mrad are now possible (e.g., Zimmermann et al., 2008; Kemna et al., 2012; Revil et al., 2012; Schmutz et al., 2014). Another key step forward has been the development of a fundamental polarization theory called the dynamic Stern layer model, that describes the underlying physics of SIP of soils (Revil et al., 2017a and references therein).

The paper is divided into three main sections. We first summarize the background theory. Then, we present a laboratory investigation regarding the relationships between the soil texture, permeability, and CEC and SIP data. Finally, we show how the SIP method can be applied in the field to image soil properties.

2. Polarization model based on the dynamic Stern layer

The complex conductivity $\sigma^{¿}$ of a soil can be characterized by its amplitude and phase lag between a sinusoidal current injected between two electrodes A and B and the potential difference measured between voltage electrodes M and N. The amplitude $|\sigma|$ (in S/m) and phase φ (in rad) can be recast into a complex-valued conductivity $\sigma^{¿}(\omega)$:

$$\sigma^{¿}(\omega)=¿\sigma\vee e^{i\varphi}=\sigma^{'}(\omega)+i\,\sigma^{''}(\omega), \quad (1)$$

where $i^2 = -1$, $\sigma^{'}$ denotes the in-phase component (S m^{-1}, associated with conduction), $\sigma^{''}$ (S/m^{-1}, associated with polarization) the quadrature conductivity (e.g., Olhoeft, 1981; Kemna et al., 2012), and $\omega = 2\,\pi\,f$ is the pulsation frequency. The polarization of a soil is associated with the ion accumulations at the grain scale because of the existence of the electrical double

143 layer around the grains (Figure 1). The Stern layer is the layer coating directly the grains and
144 formed by counterions defined as ions of opposite charge to the charge of the mineral surface.

145 The in-phase conductivity depends on two contributions corresponding to the bulk and
146 surface conductivities. At a given pulsation frequency ω (expressed in rad s^{-1}) the in-phase
147 conductivity can be expressed by (Vinegar and Waxman. 1984):

148 $$\sigma'(\omega) = \frac{1}{F} s_w^n \sigma_w + \sigma_S(s_w, \omega), \quad (2)$$

149 where σ_w (S m^{-1}) denotes the pore solution conductivity (temperature and salinity
150 dependent), , s_w (dimensionless) denotes the pore water saturation (s_w = 1 corresponds to full
151 saturation, $\theta = s_w$, ϕ denotes the dimensionless volumetric water content, ϕ, dimensionless,
152 denotes the connected porosity of the soil), F the formation factor (dimensionless) connected
153 to porosity by $F = \phi^{-m}$ (Archie's law, Archie, 1942), and σ_s (S m^{-1}) denotes the surface
154 conductivity, which depends on both saturation and frequency. The exponent m
155 (dimensionless) is called the first Archie exponent, the cementation exponent, or the porosity
156 exponent. The exponent n (dimensionless) denotes the second Archie exponent also called the
157 saturation exponent. Usually, we consider that $n \approx m$ (Revil et al., 2013b).

158 Values of the surface conductivity σ_s (in S/m) range between two limits, σ_S^0 (Direct

159 Current, DC, surface conductivity at low frequencies) and σ_S^∞ (a high-frequency asymptotic
160 value called the instantaneous surface conductivity). The frequency dependence of surface
161 conductivity is however weak (less than 10%). Low and high frequencies are defined with
162 respect to the distribution of the relaxation times characterizing the materials. These
163 relaxation times are themselves related to the distribution of characteristic length scales of the
164 porous material (typically pore or grain sizes).

In order to interpret complex conductivity spectra in a metal-free partially-saturated porous material, a model called the dynamic Stern layer model is required (e.g., Revil, 2013a, b, Revil et al., 2017a, Figure 1). Other low-frequency polarization mechanisms may exist such as membrane polarization and metallic particle polarization mechanisms (Titov et al., 2002; Revil et al., 2015a), but they are not consider to be relevant in our situation. When an harmonic electric field $\mathbf{E} = \mathbf{E}_0 \exp(+i\omega t)$ (t refers to time) is applied to a porous material, its complex conductivity is written as (Revil et al., 2017a)

$$\sigma^*(\omega) = \sigma_\infty - M_n \int_0^\infty \frac{h(\tau)}{1+(i\omega\tau)^{1/2}} d\tau \quad . \tag{3}$$

where τ is a relaxation time (in s), and $h(\tau)$ denotes a (normalized) probability density for the relaxation times of the soil. The real-valued quantity σ_∞ (S m^{-1}) corresponds to the instantaneous conductivity of the soil while the real-valued term σ_0 (S m^{-1}) corresponds to its DC (Direct Current) conductivity (Figure 1). Their expressions are further described below. The normalized chargeability M_n corresponds to the difference between the instantaneous conductivity and the DC conductivity $M_n \equiv \sigma_\infty - \sigma_0$. Note that if the chargeability is determined between two intermediate frequencies f_1 and f_2 (i.e., $M_n(f_1, f_2) = \sigma'(f_2) - \sigma'(f_1)$, $f_2 > f_1$ it is necessarily smaller than the integrated normalized chargeability $M_n \equiv \sigma_\infty - \sigma_0$ because the conductivity monotonically increases with the frequency.

Equation (3) is general. When the polarization length scales obey a log normal distribution, the complex conductivity can be expressed by a Cole Cole model

$$\sigma^* \approx \sigma_\infty \left(1 - \frac{M}{1+(i\omega\tau)^c} \right), \tag{4}$$

where c denotes the Cole Cole exponent, which describes the broadness of the density probability distribution of the relaxation times, and $M = M_n / \sigma_\infty$ (dimensionless) denotes the

chargeability. If the core samples are characterized by a bi-modal grain size distribution, we can consider that the complex conductivity is given by a double Cole Cole model In this paper, we will use such double Cole Cole model (Appendix A) to determine Cole Cole parameters for a collection of 18 soil core samples from the test site. Sometimes the soil samples can be characterized by very flat spectra (e.g., Vinegar and Waxman, 1984; Revil et al., 2017a) and in this case, it is not possible to estimate the Cole Cole parameters, and the spectra are better described by a constant phase model.

When a soil is partially saturated with a pore water electrolyte and assuming that $m \approx n$, Revil (2013a, b) obtained the following relationships:

$$\sigma_{\infty} = \theta^{m} \sigma_{w} + \theta^{m-1} \rho_{g} B \, \mathrm{CEC}, \tag{5}$$

$$\sigma_{0} = \theta^{m} \sigma_{w} + \theta^{m-1} \rho_{g} (B - \lambda) \mathrm{CEC}, \tag{6}$$

$$M_{n} = \theta^{m-1} \rho_{g} \lambda \mathrm{CEC}, \tag{7}$$

where equation (7) results from equations (5) and (6), ρ_g denotes the grain density (in kg m^{-3}), and CEC denotes the cation exchange capacity of the soil expressed in C kg^{-1} or in meq/100 g (1 meq/100 g = 963.20 C kg^{-1} in SI units), B (in m^{2}s^{-1}V^{-1}) denotes the apparent mobility of the counterions for surface conduction (associated with the in-phase conductivity) and λ (in m^{2}s^{-1}V^{-1}) denotes the apparent mobility of the counterions for the polarization associated with the quadrature conductivity (see Vinegar and Waxman, 1984). From equations (5) to (7), when the bulk water conductivity dominates the conductivity, the phase is inversely proportional to the saturation.i

A dimensionless number R was introduced by Revil et al. (2017a, b, c) as $\mathrm{R} = \lambda / B$. The two surface conductivities mentioned above are given explicitly as $\sigma_S^0 = \theta^{m-1} \rho_g (B - \lambda) \mathrm{CEC}$

and $\sigma_S'' = \theta^{m-1}\rho_g BCEC$. From Ghorbani et al. (2018), we have $B(Na^+, 25°C) = 3.1\pm0.3\times10^{-9}$ $m^2s^{-1}V^{-1}$ and $\lambda(Na^+, 25°C) = 3.0\pm0.7\times10^{-10}$ $m^2s^{-1}V^{-1}$, and $R \approx 0.10\pm0.02$.

Considering the quadrature conductivity at the geometric mean frequency of two frequencies f_1 and f_2 and the normalized chargeability defined as the difference between the in-phase conductivity at the frequency f_2(> f_1) and the in-phase conductivity at the lower frequency f_1, we can connect the quadrature conductivity and the normalized chargeability with (Van Voorhis et al., 1973; Revil et al., 2017a)

$$\sigma''\left(\sqrt{f_1 f_2}\right) \approx -\frac{M_n(f_1, f_2)}{\alpha}, \quad (8)$$

$$\alpha \approx \frac{2}{\pi}\ln A, \quad (9)$$

and A denotes the number of decades between f_1 and f_2 (for 3 decades, we have $A = 10^3$ and $\alpha \approx 4.4$). Equations (7) and (8) provide the relationship between the quadrature conductivity and the CEC. Equations (8) and (9) are not related to the dynamic Stern layer model and can be derived from the constant phase model. That said, as noticed in Revil et al. (2017a), there are very accurate for soils characterized by broad distribution of the relaxation times. From equation (8) and the expression of the surface conductivity, we can draw a relationship between the quadrature conductivity and the surface conductivity σ_S'' as

$$-\frac{\sigma''\left(\sqrt{f_1 f_2}\right)}{\sigma_S''} = \frac{M_n(f_1, f_2)}{\alpha\sigma_S''} = \frac{R}{\alpha}. \quad (10)$$

Since R and α are both two constants (independent of frequency, temperature, and saturation), this means that the quadrature conductivity and the surface conductivity are proportional to each other. Equation (10) is exact for the constant phase model, which is characterized by the absence of peaks in the quadrature conductivity spectra.

The last parameter to discuss in terms of soil property characterization is the Cole Cole relaxation time τ. According to Revil et al. (2012), we have:

$$\tau = \frac{d^2}{4m^2 D_{(+)}} \theta^2 \quad , \tag{11}$$

where $D_{(+)}$ denotes the diffusion coefficient of the counterions in the Stern layer (in m^2s^{-1}). The value of this diffusion coefficient $D_{(+)}$ is connected to the mobility of the counterions, *B*, by the Einstein relationship $D_{(+)} = k_b TB / e$, where *e* is the elementary charge, *T* denotes the absolute temperature (in K), and k_b denotes the Boltzmann constant (1.3806×10^{-23} m^2 kg s^{-2} K^{-1}). At saturation, Equation (11) reduces approximately to $\tau \approx d^2 \phi^2 / 16 D_{(+)}$ with $m \approx 2$. With equation (11) and equations (4) to (7), we can predict the effect of saturation on the shape of the spectra.

3. Laboratory investigations

3.1. Soil sample Analysis

18 soil disturbed samples were extracted with a hand auger along a 47 m transect in a vineyard located near Bordeaux (Léognan, Gironde, France). Soils along the transect are dominated by colluviosol (Baize and Girard, 1998). The samples were acquired from horizons H1 and H2 (see Figure 2) A total of 18 samples were extracted with a hand auger from the test site along the profile and at depths ranging between 0.2 to 1 m (Tregoat (2007). The samples were associated with the pedologic horizons H1, H2, and H3. Soil samples E1, E4, E5, E7, E8, E9, E12 and E17 belong to Horizon H1 (from 0 to 0.4 m). These soils are classified as sands in the GEPPA soil classification, having gravel content up to 20%, silt content up to

252 25% and clay content up to 7%. Core samples E2, E6, E10, E13, E18, E11, E14 and E19
253 belong to Horizon H2 (from 0.4 to 1 m). These samples are also classified as sand (with some
254 gravels up to 15%). The core samples E3 and E15 were extracted at a depth of 1 m at the
255 interface between Horizons H2 and H3. H2 is indicated as redoxic. The clay content in H2
256 may reach 12% and the silt fraction may range from 0 to 25%. The horizons H1, H2, and H3
257 are characterized by the presence of organic matter (0.7% in H1, 0.13% in H2, and 0.57% in
258 H3). Note that the presence of the organic matter can influence the CEC of the soil (Parfitt et
259 al., 2008). The swelling character of the soil may indicate the presence of smectite. Typical
260 grain size distribution are shon in Figure 3.

261 Additionally, a core was extracted on the profile at a depth of 3.3 m depth indicating
262 that there is no water table at least until a depth of 3 m . This core sample demonstrates the
263 existence of a compact clay layer below 1.5 m. This clay layer represents the non-calcareous
264 residue of the underlying limestones. Its existence and composition is of major importance for
265 explaining the properties of soils in the test site. Under the temperate climate of France, this
266 clay layer is rich in swelling clays like smectite (Platel et al., 2004)

267 The granulometry of each sample was determined with a MALVERN Sizer 2000 laser
268 granulometer. The sample texture is defined according to the soil texture classification of
269 GEPPA (Groupe d'Etudes des Problèmes de Pédologie Appliquée, 1963). The dark colour of
270 the shallow samples (0-0.3 m) suggests that they contain organic matter. The porosity of the
271 soil samples was estimated with weight and volume measurements. The cation exchange
272 capacity was obtained with the cobalthexamine titration method (Aran et al. 2008).

273 The pH_{H20} and pH_{KCl} measurements are done according to the NF ISO 10390 norm,
274 which specifies a method for pH measurement using a glass electrode in a suspension of soil
275 diluted 1:5 (vol. fraction) in water and in a solution of KCl at 1 mol / l (pH of KCl) or in a

solution of calcium chloride at 0.01 mol L^{-1}. The OM measurements were performed according to the NF ISO 14235 norm by sulfochromic oxidation This international standard specifies a method for the spectrometric determination of the organic carbon content in soil after oxidation in a sulfochromic medium. The properties of the core samples are summarized in Tables 1 and 2.

3.2. Laboratory SIP measurements

Frequency-domain induced polarization measurements were performed over the frequency range 10 mHz-45 kHz using the ZELSIP04-V02 impedance meter (Zimmermann et al., 2008). We use the same experimental protocol and sample holder as in Revil et al. (2017a, see Figure 4). Non-polarizable Ag/AgCl medical electrodes were used both for the current injection (electrodes A and B) and potential electrodes M and N. Some spectra are shown in Figure 5 together with the equivalent circuit model that will be used to interpret them according to the theory described in Section 2. The spectra are fitted with the double Cole Cole model described in Appendix A and the Cole Cole parameters are reported in Table 2. A fit of the spectra is shown in Figure 6.

3.3. Influence of the pore water salinity

The spectral response was measured for the 18 (disturbed) soil samples fully saturated at 3 salinities (NaCl solutions) corresponding to the following values of the electrical conductivity σ_w = 0.0720, 0.56, and 6.22 S m^{-1} (at 25°C) using protocol developed in Revil et al. (2017a). Just for completeness, we first washed the core samples, which are then saturated under vacuum with a degassed NaCl solution of determined salinity. Then the samples are stored one month to equilibrate with their solution. The volume of solution is such that the cation exchange between the pore water and the surface of the grains will not impact the conductivity of the solution. The reported conductivity is anyway the conductivity of the

300 solution measured right before prior performing the SIP spectra. Then for the two other
301 salinities, the change of pore water solutions is done by diffusion with the samples in contact
302 with a new NaCl brine to avoid desaturation of the core samples.

303 The dependence of the in-phase conductivity with the pore water conductivity (Figure
304 7) was used to invert the value of the formation factor F and surface conductivity σ_S by fitting
305 the data with equation (2) for each core sample. Then, for each sample, the cementation
306 exponent was determined from $m = -\log F / \log \theta_S$. Figure 7 shows that for low pore water
307 salinities (typically below 10^{-2} Mol L^{-1} equivalent NaCl), the (in-phase) conductivity of soils is
308 dominated by the surface conductivity because of the presence of the electrical double layer
309 surrounding the grains. The values of the formation factors and surface conductivity (at 1
310 Hertz) are reported in Table 1.

311 **3.4. Petrophysical relationships**

312 In Figure 8, the formation factor versus the (connected) porosity is plotted. The data

313 set is fitted with an Archie's law $F = \phi^{-m}$. For the samples, a typical value of the cementation
314 exponent is about $m \approx 1.71 \pm 0.10$. Then, we explore the relationship between the quadrature
315 conductivity and the surface conductivity. Both the quadrature and surface conductivity are
316 related to the electrical double layer and, according to the dynamic Stern layer model, their
317 ratio is a constant. This linear relationship is confirmed by the trend shown in Figure 9. We
318 then explore the relationship between the normalized chargeability (between 1 Hertz and 1
319 kHz) and the quadrature conductivity at the geometric frequency of 32 Hertz (see equations
320 11 and 12). As shown in Figure 10, this linear relationship is also confirmed by the
321 experimental data. The slopes of the trends show in Figures 9 and 10 can be used to estimate
322 the value of the mobilities B and λ.

3.5. Effect of the cation exchange capacity

Figures 11, 12, 13, and 14 show that the samples used in this study are consistent with other datasets made on porous rocks. Surface and quadrature conductivities are linearly related to the cation exchange capacity of the material (surface conductivity refers here to the instaneous surface conductivity, which is close to the DC surface conductivity). The dependence of the quadrature conductivity with the CEC is derived by combining equations (7) and (8). The effect of the tortuosity of the bulk pore space is shown in Figure 13 for a set of core samples with a broad range of porosity.

3.6 The relaxation time

In Figure 15, we test the relationship $\tau = d^2\phi^2 / 16 D_{(+)}$ derived from equation (11) We get a fair agreement between the model and the data with $D_{(+)} = (2.5\pm0.5)\times10^{-9}$ m^2 s^{-1}. Given that most of the core sample are sandy soils, at low frequencies (below 100 Hertz) the relaxation τ_1 primarily reflects the sand grains (Appendix A), which is much slower in principle than the relaxation of the clay particles (relaxation 2, see Appendix A). The diffusion coefficient of sodium in water is close to $D_{(+)}$ ~1.5×10^{-9} m^2 s^{-1}, a value close to the previous estimate ($D_{(+)} = (2.5\pm0.5)\times10^{-9}$ m^2 s^{-1}). Note that the Stern layer of pure silica is weak as discussed extensively in Revil (2014). In principle, the determination of the relaxation time can be useful for estimating the mean grain sizes of the coarse fraction of the core sample. For clay minerals, using d = 2 μm for clay, ϕ = 0.40 (Table 1), τ = 2x10^{-5} s (Table 2) in $D_{(+)} \approx d^2\phi^2 / 16\tau_2$ yields 2×10^{-9} m^2 s^{-1}.

4. Field application

4.1. Data acquisition

A 47.25 m-long SIP profile was acquired in the vineyard (Figure 3) June, 26 in the morning in 2017. Measurements were done after a moderate rain this day, that followed a very dry period: the cumulative curve indicates 30mm rain since June 1.

We used 64 electrodes with a spacing of 0.75 m. SIP data were acquired using an eight-channel field impedance meter DAS-1 system from Multi-Phase Technologies (MPT, http://www.mpt3d.com/das1.html). This system is based on a 24-bit A to D converter and microprocessor. In the spectral IP operating mode, the system was operated at 14 frequencies (0.125, 0.25, 0.5, 1, 1.5, 2.5, 5, 7.5, 12, 25, 37.5, 75, 112, and 225 Hz), covering therefore three orders of magnitudes. Two stacks were performed. We used a pseudo-Wenner sequence (144 measurements) and two cables, one for the current electrodes AB and one for the voltage electrodes MN (Figure 16). The voltage electrodes MN were non-polarizable electrodes while the current electrodes AB were stainless steel electrodes. The contact resistances between the electrodes and the ground was always below 3 kΩ, an acceptable value according to our experience in operating field measurements. The cables were placed approximately 40 cm above the ground to reduce capacitive coupling effects. The acquisition took 3 hours.

4.2. Dataset and tomography

We first plot the pseudo-sections of the SIP imaging data set independently for each frequency. We filtered the 5 Hz component of the dataset because of an issue with the DAS equipment, and filtered or suppressed other outliers that may have occurred. If the outlier occurs between neighbors on the phase-shift versus frequency diagram, this data point is removed out of the dataset. The phase-shift of the electrical impedance measurements generally revealed quite smooth variations in the pseudo-section in the frequency range 0.125 Hz-37.5 Hz. The phase ranged from 0.7 mrad to 10.6 mrad at 0.125 Hz, and from 0 ± 2mrad

to 20 mrad at 37.5 Hz. No filtering was necessary between 0.125 to 7.5Hz. Some isolated outliers between for 12, 25Hz had been removed, and severe filtering would have been necessary up to 37.5Hz. Up to 37.5Hz and especially up to 75Hz, many inconsistent phase-shifts occurred related to unwanted electromagnetic (EM) inductive and capacitive effects (Ghorbani et al., 2009, Schmutz et al., 2014). Capacitive effects arise due to differences in the contact resistances (i.e., between electrodes and the ground), or the conductive shields of the cables and the surface (e.g., Zimmermann et al., 2008; Zhao et al., 2013). Inductive effects are related to the current flow along the cables connecting the electrodes and the measuring devices, and their magnitude is proportional to the cable length, the electrical conductivity of the subsurface, and the frequency (e.g., Schmutz et al., 2014; Flores Orozco et al., 2018). The pseudo-Wenner sequence provided very clean data. We did not have to perform any filtering at all for the conductivity data. ~~Regarding the phase, no data were filtered out in the frequency band 0.125Hz - 2.5Hz, 5 data were removed at 7.5Hz, and 10 data were removed at 25 Hz.~~ We focus only on the first 4 m of the section for which the depth of investigation (DOI) can be determined. .

Each frequency of the whole data set was independently inverted with the code IP4DI_2D (Karaoulis et al., 2013). The (Root Mean Square Error) RMSE is in the range 2 to 5% (5% at 25Hz) depending on the frequency. A finite difference mesh was created and the covariance matrix was calculated taking into account the standard deviation of measurements. We used a Levenberg-Marquardt inversion algorithm and the Jacobian matrix was updated at each iteration. An insulating boundary condition is used at the ground surface since the normal component of the current density vanishes at the ground surface. The mesh is built in order to insure that the other boundaries mimic infinity boundary conditions for which the potential is equal to zero. The inversion converged at the 5th iteration for all the frequencies.

Once each frequency had been inverted, for each position, we developed a complex conductivity spectrum over the frequency range 0.125 to 37.5 Hz. Figure 17 shows the resulting amplitude of the conductivity and the phase at 1 Hertz and Figure 18 shows the in-phase conductivity and quadrature conductivity tomograms at the same frequency.

In order to test equations (8) and (9) on the field data, we represent the partial normalized chargeability (determined as the difference between the in-phase conductivity at 25 Hertz and 0.25 Hertz) versus the quadrature conductivity σ'' determined at the geometric mean of 2.5 Hertz, as shown in Figure 19. According to equation (9), the slope α should be 2.9. The field data exhibit a linear trend fairly consistent with this prediction with a slope close to 2.9.

In Figure 20, we compare the field data to the laboratory data at the position of the core samples E15 and E19. The observed shift between the field and laboratory data is likely due to a difference in the saturation between the laboratory experiments and the in situ conditions. Figures 20c and 20d, we observe a very good correspondence between the field and laboratory data in terms of dependence with the frequency. We can conclude from Figures 19 and 20 that the field data quality is sufficiently good and proceed with estimation of soil properties, as is described in the next section.

4.3. A strategy to estimate soil properties

Using the conductivity and phase data and equation (1), we obtain the tomograms for the in-phase and quadrature conductivities. From the quadrature conductivity, we can image the normalized chargeability $M_n = -\alpha\sigma''$ with α = 9 to include the total normalized chargeability accounting for the full range of relaxation times. Then, using equations (5) and (7) and solving a two observations (conductivity/normalized chargeability)/2 unknowns (water content, CEC) problem, we obtain:

419 $$\theta = \left[\frac{1}{\sigma_w} \left(\sigma_a - \frac{M_n}{R} \right) \right]^{1/m}, \quad (12)$$

420 $$\mathrm{CEC} = \frac{M_n}{\theta^{m-1} \rho_g \lambda}. \quad (13)$$

421 From equation (12) and (13), we estimate the water content and the CEC distributions using
422 the conductivity and normalized chargeability tomograms. Consistent with our laboratory
423 experiments on sandy samples, we use the following parameters for equations (12) and (13):

424 m = 1.71 (Figure 8), ρ_g = 2800 kg m^{-3} (average values measured on the core samples), λ

425 (15°C) =3.0±0.7×10^{-10} m^{-2}s^{-1}V^{-1}, R = 0.12, and σ_w (15°C) = 0.4 S m^{-1} representing the brackish
426 water influenced by the use of fertilizers at the site. The days before the field measurements,
427 fertilizers were indeed amended, and this was a period of heavy fertilizing because of
428 heat/moisture that might lead to grape illness. Also, it was a dry month (30 mm cumulative
429 rainfall between June 1st and June 26th day) even if the day of the measurement a moderate
430 rain occurred before the measurements (a heavy rain occurred just after the measurements).

431 The quantities m, ρ_g, R are saturation and temperature independent.

432 Figure 21 shows the tomogram of CEC and water content θ estimated using the field
433 data and equations (14) and (15). High CEC (>15 meq/100 g) values are consistent with
434 swelling clay with a high percentage of vermiculite possibly as high as 20%, which is
435 classical of a clay layer resulting from the weathering of the underlying calcareous bedrock.
436 Induced polarization can be used to estimate permeability at full or partial water saturation
437 (for instance Revil et al., 2015b). The soil permeability k (m^2) is estimated from the cation
438 exchange capacity CEC (in C kg^{-1}) and the formation factor F according to $k = k_0 (1/FQ_V)^c$
439 (Sen et al., 1990) where k_0 and c are two fitting parameters, $F = \phi^{-m}$ and

$Q_v = \rho_g (1 - \phi) \mathrm{CEC} / \phi$. This equation was validated silicoclastic geological media. According to Soueid Ahmed et al. (2020), this equation can be generalized to unsaturated conditions:

$$k \approx \frac{10^{4.3} \theta^6}{(\rho_g \mathrm{CEC})^2} \quad (14)$$

Using Equation (14) with estimates from spectral induced polarization tomography for the water content and CEC, we image the soil permeability (Figure 22). This figure reveals that the middle layer is quite impermeable (<< 1.10^{-15} m²) and may act locally as a seal.

The last step is to use the relaxation time to estimate the spatial distribution of soil mean grain size. We use the formula adapted to unsaturated conditions (see equation 11) to relate the mean grain size to the water content,

$$d = \sqrt{\frac{16 D_{(+)} \tau(\theta)}{\theta^2}}, \quad (15)$$

using $m = 2$. We apply equation (15) to each cell of the tomogram using the relaxation time inverted from the spectra and the water content from the tomogram shown in Figure 21.

At first, the agreement between the particle size fractions between the measured versus the predicted values is only fair. Obviously the support volume for the two dataset is different approximately 0.0002 m^3 for the core samples versus 0.6m^3 for the field data. That said, the main granulometric textures are well retrieved from the geophysical data with one core sample corresponding to clay (< 2μm), 3 core samples corresponding to silts (2-20 μm), and 15 core samples corresponding to fine sands (20 – 200 μm). The clay and silt fractions can only be detected thanks to the quadrature conductivity because of the frequency range used in the field. regarding the 15 core samples corresponding to fine sand according to the geophysical data,, 12 core samples are effectively in the size range observed in the laboratory (20-200 micrometers) and the 3 others are defined as coarser sands.

462 The application of equation (15) is, however, not used in areas defined by quadrature
463 conductivity > 3.5×10^{-4} S m^{-1} and in the range 2.4×10^{-4} to 3.5×10^{-4} S m^{-1} corresponding to
464 clayey and silty areas, respectively. The resulting tomogram is shown Figure 23. This figure
465 can be divided into 2 parts. The first part corresponds to the sandy soils with a subdivision
466 between fine sands and silts (20-200 μm), coarse sand (200-2000 μm), and coarse material
467 like pebbles (>2000 μm). In this part, the finest grain size (<80 μm) may not be defined if the
468 characteristic frequency occur outside of the used frequency range, or in case of uncertainty of
469 the frequency peak if data filtering/suppression should occur at the highest frequency (37.5
470 Hz) used in our study.

471 The second part of the figure corresponds to clay-silt material for which we assign the
472 value “20 μm” for silts and “2 μm” for clay, corresponding to the highest mean grain size for
473 clay and silt soil textures. We adopt this strategy as our field frequency range is restricted to a
474 narrow range. The results suggest the presence of sandy soils above and below a clay layer.
475 Also the obtained values are consistent with the values measured for the extracted samples,
476 and show an important heterogeneity of the soil texture classes. So, the relaxation times can
477 be used to infer an information regarding the grain sizes of the materials.

478 5. Discussion

479 We first summarize the procedure used in this work. We used 5 steps to estimate the
480 material properties of interest in the field. (1) We inverted the in-phase and quadrature
481 conductivities for a range of frequencies. The quadrature conductivity was transformed into a
482 normalized chargeability for each cell used to discretize the subsurface. (2) For each cell, the
483 normalized chargeability and the in-phase conductivity are used to determine the water
484 content and the CEC. (3) For each cell, the water content and the CEC are used to infer the
485 permeability. (4) The relaxation times are inverted cell by cell regarding the spectra at the

corresponding cell. (5) At each cell, the water content and the relaxation times are used to infer the mean grain size for this cell.

The CEC values inferred from the spectral induced polarization tomography data are consistent with the range of values obtained in the laboratory (see Tables 3 and 4 for a comparison). From our geophysical study, the CEC of the clay formation is found to be in the range 25-55 meq/100 g (with a mean of 43 meq/100 g). This can be compared to the CEC of a clay core samples taken inside the clay formation and characterized by a CEC in the range 40 meq/100 g (Table 4). In Figure 24, we compare the CEC determined from the geophysical data and the CEC determined from the laboratory measurements. The values are averaged for each texture (4 samples for texture SS, 8 samples for texture S1, 4 samples for textures Ls, and 1 sample for each texture LL and AA). The geophysical data are able to predict the CEC of the different textures (slope of 1.03, $r^2 = 0.93$).

The soil volumetric water content are globally low, in the range 9-25% close to the surface. The shallow moisture values are consistent with TDR measurements ranging between 15 and 25 vol.% at a 8cm depth performed at the end of June consistently with the field induced polarization measurements. During the field measurements, the weather was warm (25-30°C) and the weather was dry (30mm cumulated precipitation for the last 3.5 weeks before the field data acquisition). The water table is located at a depth of 3.5 m. The clay layer is likely water-saturated because of its high capillary pressure. The low water content of this layer means that its porosity is low because it is composed of a high density clay material.

The grain size tomography exhibits promising results since the derived grain sizes are compatible with the ones expected from the samples analysis, pedology, and core drilling (see Figure 15 and 23 and equation 15). The drilling attests that a strong swelling clay is also present at deeper depths (between 1 and 3m). We can define 3 kind of categories of grain

510 sizes. The first two are composed of clay and silt zones. They are defined through their
511 imaginary part of the conductivity values. From the laboratory data, the clay zone is defined
512 by quadrature conductivities > 3.5×10^{-4} S m^{-1} while silt areas have quadrature conductivities
513 in the range 2.4×10^{-4} and 3.5×10^{-4} S m^{-1}. The third grain size category (nine samples)
514 corresponds to fine sands with grains size typically around 100-125 μm. For these samples,
515 the calculated main grain size retrieved from spectral induced polarization tomography are
516 comprised between 101 and 233 μm, with most values between 101 and 147 μm, except for
517 sample E15 and E13 which are ~189 and 233 μm instead of 125 μm (from laser
518 measurements). Note also that a significant fraction of coarse elements may be present (or
519 even be predominant in some areas). The relaxation frequency of these coarse elements is
520 very low (between 0.25 and 5 Hz) outside the range investigated in the present study. In the
521 future, and to get a broader grain size distribution from SIP tomography, the frequency range
522 in the field the use of lower and higher frequencies should be considered.

523 Finally, a fundamental question is to know if, in field conditions, surface conductivity
524 is negligible or not since in a large number of studies in hydrogeophysics, surface
525 conductivity is neglected without any discussion about this point. In Figure 25, we plot from
526 the field data at the position of the core sample the normalized chargeability (from the
527 inversion of the spectra) versus the instantaneous conductivity. The slope being close to R =
528 0.13 (Figure 25a), this indicates that for the field conditions, surface conductivity dominates
529 the conductivity response in the field (if this is not the case, the slope should be smaller than
530 R). In Figure 25b, we plot some of the laboratory data in which the conductivity of the core
531 samples is plotted as a function of the conductivity of the pore water. We add the range of
532 plausible pore water conductivities in the field conditions. We see clearly that surface
533 conductivity is extremely important in the overall conductivity response of these sandy soils.

534 Therefore the application of a conductivity equation neglecting surface conduction would be
535 erroneous.
536

537 ## 6. Conclusion

538 Spectral Induced Polarization (SIP) in the frequency range 0.25-25 Hertz is a powerful
539 geophysical method to image soil properties. We apply here the dynamic Stern layer model of
540 induced polarization of Revil et al. (2017a) to a new dataset of soils from a Bordeaux
541 vineyard. The experimental data are consistent with the dynamic Stern layer model and
542 theory. The analysis is performed for the surface conductivity, the quadrature conductivity
543 and normalized chargeability, and the main relaxation times using a Cole Cole complex
544 conductivity model. From these results, a strategy was developed to interpret field data. We
545 acquired field spectral induced polarization measurements in the frequency range 0.125 Hz to
546 75 Hz. The quality of the field data set was further checked by looking at the relationship
547 between the normalized chargeability (between 0.25 Hertz and 25 Hertz) and the quadrature
548 conductivity at 2.5 Hertz. Some comparisons were also made by comparing the field spectra
549 and the experimental data at 2 locations where core samples were extracted. Finally, the field
550 data were used to image the water content, the Cation Exchange Capacity, the mean grain
551 size, and the permeability down to a depth of 4 meters and validation stems from the first
552 meter of the subsurface. A shallow smectite-rich clay layer is identified and characterized.
553 To the best of our knowledge, this is the first field scale estimation of CEC, grain size,
554 water content, and permeability using spectral induced polarization tomography in soils. That
555 said, the quality of predictions need to further assessed in future studies embracing more
556 divers environments, soil use (e.g., including roots) and combined with soil measurements
557 The present study confirms also the applicability of the dynamic Stern layer model to

558 understand induced polarization of soils in terms of fundamental physicochemical parameters.
559 We have shown that surface conductivity cannot be neglected in the field. Spectral induced
560 polarization tomography can be now used for agricultural purpose and the study of the critical
561 zone and the method needs to be improved to higher frequencies. The present approach has
562 assumed that sodium was the main counterions in the Stern layer. The influence of
563 heterogeneity in the chemistry of the soil samples could be accounted for. In irrigated fields,
564 heterogeneous distribution of chemical species (especially in the vertical direction) can occur
565 and a more complex dynamic Stern layer model should be applied as shown by Vaudelet et al.
566 (2011a, b).
567
568 **Acknowledgements.** We thank the INTERREG SUDOE project "Soil Take Care" for
569 funding. and the Chateau "La Louviere" in France for access to their domain. The authors are
570 grateful to C. Arbogast for his help in the field. S. Hubbard was supported through the
571 Watershed Function Scientific Focus Area funded by the U.S. Department of Energy, Office
572 of Science, Office of Biological and Environmental Research under Award Number DE-
573 AC02-05CH11231. The data are provided in DRYAD
574 (https://doi.org/10.5061/dryad.n02v6wwvs). We thank the Editor, Dr. Cristine Morgan, and
575 three anonymous referees for their very useful comments.
576

References

Abdulsamad, F., Revil, A., Soueid Ahmed, A., Coperey, A., Karaoulis, M., Nicaise, S., Peyras, L., 2019. Induced polarization tomography applied to the detection and the monitoring of leaks in embankments. Engineering Geology 254, 89-101. https://doi.org/10.1016/j.enggeo.2019.04.001.

AcclimaTerra, Le Treut, H. (2018). Anticiper les changements climatiques en Nouvelle-Aquitaine. Pour agir dans les territoires. Éditions Région Nouvelle-Aquitaine, 488 pp.

Altdorff, D., von Hebel, C., Borchard, N., van der Kruk, J., Bogena, H.R., Vereecken, H. and Huisman, J.A. (2017). Potential of catchment-wide soil water content prediction using electromagnetic induction in a forest ecosystem. Environ Earth Sci. 76(111). https://doi.org/10.1007/s12665-016-6361-3.

André, F., Saussez, S., Moghadas, D., Van Durmen, R., Delvaux, B., Vereecken, H., Lambot, S., de Rességuier, L., Van Leeuwen, C., and Bogaert, P. (2012). High-Resolution Imaging of a Vineyard in South of France Using Ground-Penetrating Radar, Electromagnetic Induction and Electrical Resistivity Tomography. Journal of Applied Geophysics, 78, 113–22.

Aran, D., Maul, A., and Masfaraud, J.F. (2008). A spectrophotometric measurement of soil cation exchange capacity based on cobaltihexamine chloride absorbance. Comptes Rendus Geoscience, 340(12), 865–871. https://doi.org/10.1016/j.crte.2008.07.015.

Archie, G. E. (1942). The electrical resistivity log as an aid in determining some reservoir characteristics. SPE-942054-G, 146, 54–62. https://doi.org/10.2118/942054-G.

Arya, L.M. and Paris, J.F. (1981). A Physicoempirical Model to Predict the Soil Moisture Characteristic from Particle-Size Distribution and Bulk Density Data. Soil Science Society of America Journal, 45(6), 1023-1030.

https://doi.org/10.2136/sssaj1981.03615995004500060004x.XBaize, D., and Girard, M. (1998). A Sound Reference Base for Soils: The "Référentiel Pédologique". Institut National de La Recherche Agronomique, Paris, Editors.

Bolève, A., Crespy, A., Revil, A., Janod, F., and Mattiuzzo, J. L. (2007). Streaming potentials of granular media: Influence of the Dukhin and Reynolds numbers. J. Geophys. Res. 112, B08204. https://doi.org/10.1029/2006JB004673.

Börner, F. D. (1992). Complex conductivity measurements of reservoir properties, Proceedings of the Third European Core Analysis Symposium, Paris, 359-386.

Brunet, P., Clément, R. and Bouvier C. (2010). Monitoring soil water content and deficit using Electrical Resistivity Tomography (ERT) – A case study in the Cevennes area, France. Journal of Hydrology, 380(1-2), 146-153. https://doi.org/10.1016/j.jhydrol.2009.10.032

Churcher, R.L., French, P.R., Shaw, J.C., and Schramm, L.L. (1991). Paper SPE 21041 presented at the 1991 Int. Symp. On Oilfield Chemistry, Anaheim, February 20-22.

Cnudde, V., and Boone, M. N. (2013). High-resolution X-ray computed tomography in geosciences: A review of the current technology and applications. Earth-Science Reviews, 123, 1-17.

Comparon L. (2005). Etude expérimentale des propriétés électriques et diélectriques des matériaux argileux consolidés. PhD Thesis, Institut de Physique du Globe de Paris 400 pp. https://hal.archives-ouvertes.fr/tel-00135855/.

Dukhin S.S., and Shilov V.N. (1974). Dielectrical phenomena and the double layer in disperse systems and polyelectrolytes. Wiley, New York.

623 Dumanski, J., and Peiretti, R., (2013). Modern concepts of soil conservation International Soil
624 and Water Conservation Research 1(1), 19-23. https://doi.org/10.1016/S2095-
625 6339(15)30046-0**.**
626 Eckhart, V.M., Howland
627 , M.R., Jennison, K., Kircher, B.K., Montgomery, D.M., Yuan, Y. and Geber M.A. (2017).
628 Contrasting soil-texture niches facilitate coexistence of two congeneric plants that differ
629 in competitive ability. *AoB PLANTS*, 9(6), plx066. https://doi.org/10.1093/aobpla/plx066.
630 Fixman, M., (1980), Charged macromolecules in external fields. I. the sphere: Journal of
631 Chemical Physics, 72(9), 5177–5186, https://doi.org/10.1063/1.439753.
632 Flores Orozco, A., Bücker, M., Steiner, M., and Malet, J-P. (2018). Complex conductivity
633 imaging for the understanding of landslide architecture. Eng. Geology 243, 241-252.
634 Friedman, S.P., (2005). Soil properties influencing apparent electrical conductivity: a review,
635 Computers and Electronics in Agriculture, 46(1-3), 45-70.
636 https://doi.org/10.1016/j.compag.2004.11.001.
637 Gardner, W.H. (1986). Methods of Soil Analysis: Part 1 Physical and Mineralogical Methods,
638 5.1. Second Edition : Book Editor(s): Arnold Klute, Book Series:SSSA Book Series,
639 chap. 21. https://doi.org/10.2136/sssabookser5.1.2ed.c21.
640 Gebbers, R., and Adamchuk, V.I. (2010). Precision Agriculture and Food Security. Science,
641 327, 828-831. https://doi.org/10.1126/science.1183899.
642 Ghanbarian, B., Hunt, A.G., Skaggs, T.H. and Jarvis, N. (2017). Upscaling soil saturated
643 hydraulic conductivity from pore throat characteristics. Advances in Water Resources,
644 104, 105-113. https://doi.org/10.1016/j.advwatres.2017.03.016.
645 Ghorbani, A., Camerlynck, C. and Florsch, N. (2009). CR1Dinv: A Matlab program to invert
646 1D spectral induced polarization data for the Cole–Cole model including electromagnetic

effects. Computer and Geosciences, 35(2), 255-266. https://doi.org/10.1016/j.cageo.2008.06.001

Ghorbani, A., Revil, A., Coperey, A., Soueid Ahmed, A., Roque, S., Heap, M. J., Grandis, H. and Viveiros, F. (2018). Complex conductivity of volcanic rocks and the geophysical mapping of alteration in volcanoes. Journal of Volcanology and Geothermal Research, 357, 106–127. https://doi.org/10.1016/j.jvolgeores.2018.04.014.

Gouy, G. L. (1910). Sur la constitution de la charge électrique à la surface d'un électrolyte: Journal de Physique Théorique et Appliquée, 9, 457–468. https://doi.org/10.1051/jphystap:019100090045700.

Grote, K., Anger, C., Kelly, B., Hubbard, S. and Rubin, Y., (2010). Characterization of Soil Water Content Variability and Soil Texture using GPR Groundwave Techniques. Journal of Environmental and Engineering Geophysics, 15(3), https://doi.org/10.2113/JEEG15.3.93.

Hazelton, PA. and Murphy, BW. (2007). Interpreting Soil Test Results: What do all the numbers mean? CSIRO Publishing: Melbourne.

Huisman, J. A., Hubbard, S.S., Redman, J.D., and Annan, A.P. (2003). Measuring Soil Water Content with Ground Penetrating Radar. Vadose Zone Journal, 2(4), 476-491.

Ikard, S., Revil, A., Schmutz, M., Karaoulis, M., Jardani, A., and Mooney, M. (2014). Characterization of focused seepage through an earthfill dam using geoelectrical methods: Groundwater, 52 (6), 952-965.

IPCC Special Report on Climate Change and Land (2019). An IPCC Special Report on climate change, desertification, land degradation, sustainable land management, food security,and greenhouse gas fluxes in terrestrial ecosystems. Eds: V. Masson-Delmotte, P. Zhai, H.-O. Pörtner, D. Roberts, J. Skea, E. Calvo, B. P.R. Shukla, R. Slade, S.

Connors, R. van Diemen, M.Ferrat, E. Haughey, S. Luz, S. Neogi, M. Pathak, J. Petzold, J. Portugal, P. Purvi, V. E. Huntley, K. Kissick, M. Belkacemi, J. Malley. 874 pp.

Jafarzadeh, A. A., Pal, M., Servati, M., FazeliFard, M. H., and Ghorbani, M. A. (2016). Comparative analysis of support vector machine and artificial neural netw.ork models for soil cation exchange capacity prediction: International Journal of Environmental Science and Technology, 13, 87–96. https://doi.org/10.1007/s13762-015-0856-4.

Karaoulis, M., Revil, A., Tsourlos, P., Werkema, D.D., and Minsley, B.J. (2013). IP4DI: A software for time-lapse 2D/3D DC-resistivity and induced polarization tomography. Computers and Geosciences, 54, 164-170. https://doi.org/10.1016/j.cageo.2013.01.008.

Kemna, A., Binley, A., Cassiani, G., Niederleithinger, E., Revil, A., Slater, L., Williams, K.H., Flores Orozco, A., Haegel, F.-H., Hördt, A., Kruschwitz, S., Leroux, V., Titov, K. and Zimmermann, E. (2012). An overview of the spectral induced polarization method for near-surface applications. Near Surface Geophysics, 10, 453-468. https://doi.org/10.3997/1873-0604.2012027.

Kurniawan, B. (2005). Shaly sand interpretation using CEC-dependent petrophysical parameters. PhD Thesis, Louisiana State University, 201 pp. https://digitalcommons.lsu.edu/gradschool_dissertations/2384.

Lambe T. W., (1955). The Permeability of Fine-Grained Soils, in *Symposium on Permeability of Soils*, ed. R. Subcommittee (West Conshohocken, PA: ASTM International), 56-67. https://doi.org/10.1520/STP46165S.

Legchenko, A., Baltassat, J.-M., Beauce, A. and Bernard, J. (2002). Nuclear magnetic resonance as a geophysical tool for hydrogeologists: Journal of Applied Geophysics, 50(1-2), 21-46. https://doi.org/10.1016/S0926-9851(02)00128-3.

694 Li, N., Zare, E., Huang, J., & Triantafilis, J. (2018). Mapping soil cation-exchange capacity
695 using Bayesian modeling and proximal sensors at the field scale. Soil Science Society of
696 America Journal, 82(5), 1203-1216. https://doi.org/10.2136/sssaj2017.10.0356.
697 Lorne, B., Perrier, F., and Avouac, J.-P. (1999). Streaming potential measurements. 1.
698 Properties of the electrical double layer from crushed rock samples. Journal of
699 Geophysical Research, 104(17), 857-877. https://doi.org/10.1029/1999JB900156.
700 Martinez, G., Huang, J., Vanderlinden, K., Giráldez, J. V., & Triantafilis, J. (2018). Potential
701 to predict depth-specific soil-water content beneath an olive tree using electromagnetic
702 conductivity imaging. Soil Use and Management, 34(2), 236-248.
703 https://doi.org/10.1111/sum.12411.
704 Mosegaard, K., and Tarantola, A. (1995). Monte Carlo sampling of solutions to inverse
705 problems. Journal of Geophysical Research, 100, no. B7, 12431–12447,
706 https://doi.org/10.1029/94JB03097.
707 Muzzamal M; Huang J; Nielson R; Sefton M; Triantafilis J. (2018). Mapping soil particle-size
708 fractions using additive log-ratio (ALR) and isometric log-ratio (ILR) transformations
709 and proximally sensed ancillary data. Clays and Clay Minerals, 66, 9-27,
710 http://dx.doi.org/10.1346/CCMN.2017.064074.
711 Oliver, D. P., Bramley, R. G. V., Riches, D., Porter, I., and Edwards, J. (2013). Review: soil
712 physical and chemical properties as indicators of soil quality in Australian viticulture.
713 Australian Journal of Grape and Wine Research, 19(2), 129-139. https://doi.org/10.1111/
714 ajgw.12016.
715 Olhoeft, G.R. (1981). Electrical Properties of Rocks. Physical properties of rocks and
716 minerals. 17p.

717 Parfitt, R.L., Giltrap, D.J., and Whitton, J.S. (1995). Contribution of organic-matter and clay-
718 minerals to the cation-exchange capacity of soils: Communications in Soil Science and
719 Plant Analysis, 26, 1343–1355.
720 Parfitt, R.L., Giltrap, D;J., and Whitton, J.S., (2008). Contribution of organic matter and clay
721 minerals to the cation exchange capacity of soils, Communications in Soil Science and
722 Plant Analysis, 26(9-10), 1343-1355. https://doi.org/10.1080/00103629509369376.
723 Pennington, V.E., Palmquist, K.A., Bradford, J.B., and Lauenroth, W.K. (2017). Climate and
724 soil texture influence patterns of forb species richness and composition in big sagebrush
725 plant communities across their spatial extent in the western U.S. Plant ecology, 218, 957–
726 970.
727 Petersen, H., Fleige, H., Rabbel, W. and Horn, R. (2005). Applicability of geophysical
728 prospecting methods for mapping of soil compaction and variability of soil texture on
729 farm land. Journal of Plant Nutrition and Soil Science-Zeitschrift Fur Pflanzenernahrung
730 Und Bodenkunde, 168 (1). pp. 68-79. https://doi.org/10.1002/jpin.2004.21282.
731 Platel, J.P., Esteve, A. and Tomera, L. (2004). Cartographie de l'aléa retrait-gonflement des
732 argiles dans le département de la Gironde. Rapport final. BRGM/RP-53382-FR, 236 pp.
733 Revil, A., Darot, M., Pezard, P.A., and Becker, K. (1996). Electrical conduction in oceanic
734 dikes, Hole 504B, Ed. by Alt, J.C., Kinoshita, H., *et al*., Proc. ODP Sci. Res., 148,
735 College Station, TX (ODP), 297-305.
736 Revil, A., Cathles, L.M., Losh, S., and Nunn, J.A. (1998). Electrical conductivity in shaly
737 sands with geophysical applications, Journal of Geophysical Research, 103(B10), 23,925-
738 23,936.

739 Revil, A., Hermitte, D., Spangenberg, E., and Cochémé, J. J. (2002). Electrical properties of
740 zeolitized volcaniclastic materials. Journal of Geophysical Research, 107(B8), 2168.
741 https://doi.org/10.1029/2001JB000599.
742 Revil, A., Karaoulis, M., Johnson, T., and Kemna, A. (2012). Review: Some low-frequency
743 electrical methods for subsurface characterization and monitoring in hydrogeology.
744 Hydrogeology Journal, **20(4)**, 617–658. https://doi.org/10.1007/s10040-011-0819-x.
745 Revil, A. (2013a). On charge accumulation in heterogeneous porous rocks under the influence
746 of an external electric field. Geophysics, 78(4), D271–291.
747 https://doi.org/10.1190/geo2012-0503.1.
748 Revil, A., (2013b). Effective conductivity and permittivity of unsaturated porous materials in
749 the frequency range 1mHz-1GHz. Water Resour. Res., 49, 306-327.
750 https://doi.org/10.1029/2012WR012700.
751 Revil., A. (2014). Comment on: "On the relationship between induced polarization and
752 surface conductivity: Implications for petrophysical interpretation of electrical
753 measurements" (A. Weller, L. Slater, and S. Nordsiek, Geophysics, 78, no. 5, D315–
754 D325), Geophysics, 79, no. 2, X1-X5, doi: 10.1190/GEO2013-0300.1.
755 Revil A., N. Florsch, and D. Mao (2015a). Induced polarization response of porous media
756 with metallic particles — Part 1: A theory for disseminated semiconductors. Geophysics,
757 80(5), D525–D538. https://doi.org/10.1190/GEO2014-0577.1.
758 Revil, A., Binley, A., Mejus, L., and Kessouri, P. (2015b). Predicting permeability from the
759 characteristic relaxation time and intrinsic formation factor of complex conductivity
760 spectra: Water Resour. Res., 51. https://doi.org/10.1002/2015WR017074.

761 Revil, A., Coperey, A., Shao, Z., Florsch, F., Fabricius, L. I., Deng, Y., and Delsman, J. R.
762 (2017a). Complex conductivity of soils. Water Resources Research, 53(8), 7121–47.
763 https://doi.org/10.1002/2017WR020655.
764 Revil A., Le Breton, M., Niu, Q., Wallin, E., Haskins, E., and Thomas, D.M. (2017b).
765 Induced polarization of volcanic rocks. 1. Surface versus quadrature conductivity.
766 Geophysical Journal International, 208, 826–844. https://doi.org/10.1093/gji/ggw444.
767 Revil, A., Le Breton, M., Niu, Q., Wallin, E., Haskins, E., and Thomas, D.M. (2017c).
768 Induced polarization of volcanic rocks. 2. Influence of pore size and permeability.
769 Geophysical Journal International, 208, 814–825. https://doi.org/10.1093/gji/ggw382.
770 Revil, A., Coperey A., Deng Y., Cerepi A., and Seleznev, N. (2018a), Complex conductivity
771 of tight sandstones, Geophysics, 83, 2, E55-E74.. https://doi.org/10.1190/GEO2017-
772 0096.1.
773 Revil A., Y. Qi, A. Ghorbani, A. Soueid Ahmed, T. Ricci, and P. Labazuy (2018b), Electrical
774 conductivity and induced polarization investigations at Krafla volcano, Iceland, Journal
775 of Volcanology and Geothermal Research, 368, 73–90. https://doi.org/10.1016
776 /j.jvolgeores.2018.11.008.
777 **Re**vil A., Qi Y., Ghorbani A., Gresse M., and Thomas D.M. (2021), Induced polarization of
778 volcanic rocks. 5. Imaging the temperature field of shield volcanoes: Geophys. J. Int.,
779 225, 1492–1509, https://doi.org/10.1093/gji/ggab039.
780 Robinet, J., von Hebel, C., Govers, G., van der Kruk, J., Minella, J. P. G., Schlesner, A.,
781 Ameijeiras-Marino, Y., and Vanderborght, J. (2018). Spatial variability of soil water
782 content and soil electrical conductivity across scales derived from Electromagnetic
783 Induction and Time Domain Reflectometry: Geoderma, 314, 160-174.

784 Rubin, M. and Hubbard, S.S. (2005). Hydrogeophysics. Water Science and Technology
785 Library, 50, 518 pp.
786 Sainju, U. M., and Singh, P. (1997). Winter cover crops for sustainable agricultural systems:
787 influence on soil properties, water quality, and crop yields. Hort Science, 32(1), 21-28.
788 Sen, P. N., Straley, C., Kenyon, W. E., and Whittingham, M. S. (1990). Surface-to-volume
789 ratio, charge density, nuclear magnetic relaxation, and permeability in clay-bearing
790 sandstones. Geophysics, 55(1), 61-69.
791 Schmutz, M., Ghorbani, A., Vaudelet, P., and Blondel, A. (2014). Cable arrangement to
792 reduce electromagnetic coupling effects in spectral-induced polarization studies.
793 Geophysics, **79(**2). https://doi.org/10.1190/geo2013-0301.1.
794 Shah P. and D. Singh (2005). Generalized Archie's law for estimation of soil electrical
795 conductivity, Journal of ASTM International 2(5), 1-
796 20. https://doi.org/10.1520/JAI13087.
797 Soueid Ahmed, A., Revil, A., Abdulsamad, F., Steck, B., Vergniault, C., and Guihard, V.
798 (2020). Induced polarization as a tool to non-intrusively characterize embankment
799 hydraulic properties. Engineering Geology, 271, 105604,
800 https://doi.org/10.1016/j.enggeo.2020.105604.
801 Stern, O. (1924). Zur Theorie der elektrolytischen doppelschicht, 30, 21-22, 508-516,
802 https://doi.org/10.1002/bbpc.192400182.
803 Titov, K., Komarov, V., Tarasov, V., Levitski, A. (2002). Theoretical and experimental study
804 of time domain-induced polarization in water-saturated sands, J. Appl. Geophys. ,50 (4),
805 417–433. http://dx.doi.org/10.1016/S0926-9851(02)00168-4.
806 Topp, G.C. (2003). State of the art of measuring soil water content. Hydrol. Process. 17,
807 2993–2996.

Tregoat, O. (2007). Cartographie des sols du vignoble de Château la Louviere. Carte pédologique et notice, 52 pp.

Van Voorhis, G. D., Nelson P. H., and Drake T. L. (1973). Complex resistivity spectra of porphyry copper mineralization. Geophysics, 38(1), 49–60. https://doi.org/10.1190/1.1440333.

Van Leeuwen, C. (2010). Soils and terroir expression in wines. In: Landa E., Feller C. (eds) Soil and Culture. Springer, Dordrecht, 453-465. https://doi.org/10.1007/978-90-481-2960-7_28.

Vaudelet P., A. Revil, M. Schmutz, M. Franceschi, and P. Bégassat (2011a). Induced polarization signature of the presence of copper in saturated sands, Water Resources Research, 47, W02526, doi:10.1029/2010WR009310.

Vaudelet P., Revil, A., M. Schmutz, M. Franceschi, and P. Bégassat, 2011b. Changes in induced polarization associated with the sorption of sodium, lead, and zinc on silica sands, Journal of Colloid and Interface Science, 360, 739-752.

Vinegar, H., and Waxman, M. (1984). Induced polarization of shaly sands. Geophysics, 49(8), 1267–87. https://doi.org/10.1190/1.1441755.

Weller, A., Slater, L., and Nordsiek, S. (2013). On the relationship between induced polarization and surface conductivity: Implications for petrophysical interpretation of electrical measurements. Geophysics, 78(5), D315–D325. https://doi.org/10.1190/geo2013-0076.1.

Yolcubal, I., Brusseau, M.L., Artiola, J.F., Wierengal, P., and Wilson, G. (2004). Environmental physical properties and processes. Environmental monitoring and characterization, 207-239.

831 Zare, E., Arshad, M., Zhao, D., Nachimuthu, G., & Triantafilis, J. (2020). Two-dimensional
832 time-lapse imaging of soil wetting and drying cycle using EM38 data across a flood
833 irrigation cotton field. Agricultural Water Management, 241.
834 https://doi.org/10.1016/j.agwat.2020.106383
835 Zhao, D., Li, N., Zare, E., Wang, J., & Triantafilis, J. (2020a). Mapping cation exchange
836 capacity using a quasi-3d joint inversion of EM38 and EM31 data. Soil and Tillage
837 Research, 200. https://doi.org/10.1016/j.still.2020.104618.
838 Zhao, X., Arshad, M., Li, N., Zare, E., & Triantafilis, J. (2020b). Determination of the
839 optimal mathematical model, sample size, digital data and transect spacing to map CEC
840 (Cation exchange capacity) in a sugarcane field. Computers and Electronics in
841 Agriculture, 173. https://doi.org/10.1016/j.compag.2020.105436.
842 Zhao, Y., Zimmermann, E., Huisman, J. A., Treichel, A., Wolters, B., van Waasen, S., and
843 Kemna, A. (2013). Broadband EIT borehole measurements with high phase accuracy
844 using numerical corrections of electromagnetic coupling effects. Measurement Science
845 and Technology, 24(8), 085005.
846 Zimmermann, E., Kemna, A., Berwix, J., Glaas, W., Münch, H. M., and Huisman, J. A.
847 (2008). A high-accuracy impedance spectrometer for measuring sediments with low
848 polarizability. Measurement Science and Technology, 19(10), 105603.
849 https://doi.org/10.1088/0957-0233/19/10/105603.
850

Appendix A. Inversion of the Cole Cole parameters

We consider that the grain size distribution is bimodal with coarse grains (sands) and small grains (clays). The corresponding double Cole-Cole equation is written as

$$\sigma^* = \sigma_\infty \left(1 - \frac{M_1}{1 + (i\omega\tau_1)^{c_1}} - \frac{M_2}{1 + (i\omega\tau_2)^{c_2}} \right) \quad \text{(A1)}$$

where M_1 and M_2 denote the chargeabilities, c_1 and c_2 are the two Cole-Cole exponents (dimensionless), and τ_1 and τ_2 are the (relaxation) time constants (in s). The index 1 and 2 refer to lower (sand) and higher (clay) frequency dispersions, respectively. The (integrated or total) normalized chargeability M_n is obtained as $M_n = \sigma_\infty (M_1 + M_2)$.

The complex conductivity spectra can be inverted using equation (A1) and the non-linear iterative approach of Mosegaard and Tarantola (1995) based on a Monte Carlo Markov Chain (MCMC) sampling algorithm. The Bayesian approach describes the prior information we have on the model vector, using a probability density P(**m**) where **m** denotes the model vector of unknown parameters **m** = [log(σ_0); M_1; c_1; log(τ_1); M_2; c_2; log(τ_2)]. Then, the algorithm combines this information with the observed data vector $\mathbf{d}_{obs}$ and with the information provided by the double Cole-Cole model, L(**m**), as described by equation (A1). In Bayesian theory, the posterior probability density σ(**m**) equals the prior probability density P(**m**) times a likelihood function L(**m**), which measures the fit between observed data and data predicted from the model vector **m**, i.e, $\sigma(\mathbf{m}) = hP(\mathbf{m})L(\mathbf{m})\ \sigma(m) = k \cdot P(m) \cdot L(m)$, where h denotes a normalization constant. We describe the complex conductivity data by a vector of observed values $\mathbf{d}_{obs}$ characterized by Gaussian uncertainties associated with the measurement procedure. We consider the case of independent, identically distributed Gaussian

uncertainties. Then the likelihood function describing the experimental uncertainties is given by:

$$L(\mathbf{m}) = k \exp\left(- \frac{S(\mathbf{m})}{s^2} \right) \quad L(m) = k \cdot \exp\left[\frac{-S(m)}{s^2} \right], \tag{A2}$$

where s^2 is the total noise variance and where the misfit function is given by

$$S(m) = \frac{1}{2} \sum_{i=1}^{n} \left(g^i(m) - d_{obs}^i \right)^2 \quad S(\mathbf{m}) = \frac{1}{2} \sum_{i=1}^{n} \left(g^i(\mathbf{m}) - d_{obs}^i \right)^2, \tag{A3}$$

where **d** is data vector, $g(\mathbf{m})=\sigma^*$ is the forward modeling function, and s^2 is the same for all data values. The acceptance probability for a perturbed model becomes

$$P_{accept} = \begin{cases} 1 \text{ if } S(\mathbf{m}_{new}) \le S(\mathbf{m}_{old}) \\ \exp\left(- \frac{\Delta S}{s^2} \right) \text{ if } S(\mathbf{m}_{new}) > S(\mathbf{m}_{old}) \end{cases} \quad P_{accept} \begin{cases} 1 \; if \; S(m_{new}) \le S(m_{old}) \\ \exp\left(\frac{-\Delta S}{s^2} \right) if \; S(m_{new}) > S(m_{old}) \end{cases} \tag{A4}$$

where $\Delta S = S(\mathbf{m}_{new}) - S(\mathbf{m}_{old})$. The observed data used in the inversion process were the real and imaginary parts of the complex conductivity calculated from the amplitude and phase values measured at different frequencies.

We assume that the standard deviation, *s*, is equal to 10% of the measured complex conductivity values (i.e., corresponding to the maximum of the experimental error). Locally uniform law (the probability distribution is constant over an interval $[\theta_1, \theta_2]$ and vanishes elsewhere) is used to describe the prior probability density on the model parameters. Interval ranges for Cole-Cole model parameters are: $\sigma_0 = [10^{-4}; 100]$ S m^{-1}, M_1 and M_2, c_1 and c_2 have the same interval [0 1], $\tau_1=[10^{-5}, 10^5]$ s, and $\tau_2=[10^{-15}, 10^{-4}]$ s. At the end of the inversion algorithm, we compute the Root Mean Square (RMS) error:

$$RMS = \sqrt{\frac{1}{n} \cdot \left[\frac{\sum_{i=1}^{n} \left(g^i(m) - d_{obs}^i \right)^2}{d_{obs}^i} \right]} \qquad \mathrm{RMS}^2 = \frac{1}{n} \sum_{i=1}^{n} \left(\frac{g^i(\mathbf{m}) - d_{obs}^i}{d_{obs}^i} \right)^2, \tag{A5}$$

where *n* denotes the number of measurements. The results are reported in Table 2.

Tables

Table 1. Physiochemical properties of the core samples. The quadrature conductivity σ" is reported at 32 Hertz (samples E1 to E19, pore water conductivity of 0.072 S m^{-1} at 25°C, NaCl, sample REM pore water conductivity of 0.12 S m^{-1} at 25°C, NaCl). There is no sample labeled E16. The quantity ϕ denotes the porosity, CEC denotes the Cation Exchange Capacity, F denotes the formation factor, σ_S denotes the surface conductivity, M_n(1 Hz, 1 kHz) is the (partial) normalized chargeability determined at the lowest salinity and between 1 Hertz and 1 kHz. The main grain size corresponds to the peak of the distribution.

Core ID	ϕ (-)	CEC (meq/ 100g)	F (-)	σ_S (S/m)	M_n(1 Hz, 1 kHz) (S/m)	σ" (S/m)	Main grain size (μm)
E1	0.35	11.9	4.97	0.042	0.0049	0.0010	105
E2	0.36	9.53	5.80	0.032	0.0026	0.0006	98
E3	0.36	7.21	3.97	0.0107	0.0010	0.0003	63
E4	0.39	16.1	6.66	0.0771	0.0054	0.0013	88
E5	0.44	16.6	5.71	0.0932	0.0036	0.0008	40
E6	0.41	15.5	5.90	0.092	0.0055	0.0012	40
E7	0.39	7.82	3.84	0.0565	0.0034	0.0007	4
E8	0.43	7.24	3.54	0.0333	0.0021	0.0005	8
E9	0.42	11.5	3.16	0.0352	0.0025	0.0002	101
E10	0.43	7.67	5.40	0.0603	0.0027	0.0006	8
E11	0.40	7.3	4.18	0.0384	0.0021	0.0005	100
E12	0.51	20	4.89	0.114	0.0090	0.0021	40
E13	0.52	19.9	2.77	0.0503	0.0036	0.0014	125
E14	0.44	15.8	4.73	0.085	0.0054	0.0012	125
E15	0.43	9.77	6.65	0.155	0.0062	0.0019	125
E17	0.48	17.9	3.97	0.260	0.0147	0.0041	75
E18	0.45	12.3	7.24	0.186	0.0073	0.0017	93
E19	0.44	11.5	2.94	0.0031	0.0003	0.0004	125
REM	0.26	2.6	9.10	0.031	0.00024	0.00085	-

904 **Table 2.** Double Cole Cole parameters obtained for the core samples at the lowest salinity.

Core ID	σ_∞ (S/m)	M_1 (-)	M_2 (-)	c_1 (-)	c_2 (-)	τ_1 (s)	τ_2 (s)	RMS (%)	Texture GPA [1]
E1	0.060	0.094	0.034	0.442	0.482	0.032	5.7e-05	0.19	SS
E2	0.045	0.062	0.069	0.409	0.466	0.020	2.3e-05	0.11	SS
E3	0.032	0.066	0.098	0.357	0.492	0.011	2.3e-06	0.24	Sl
E4	0.082	0.085	0.049	0.407	0.473	0.021	4.6e-05	0.16	SS
E5	0.099	0.041	0.091	0.320	0.470	0.008	7.4e-06	0.16	Ls
E6	0.107	0.068	0.075	0.351	0.514	0.015	1.4e-05	0.14	Ls
E7	0.082	0.034	0.089	0.371	0.395	0.063	1.3e-05	0.23	LL
E8	0.059	0.019	0.069	0.465	0.469	0.113	8.9e-05	0.25	Ls
E9	0.020	0.053	0.072	0.462	0.481	0.035	2.2e-06	0.74	SS
E10	0.075	0.043	0.111	0.369	0.420	0.019	20e-06	0.35	Sl
E11	0.059	0.029	0.091	0.446	0.463	0.072	1.1e-05	0.46	Sl
E12	0.120	0.089	0.061	0.446	0.642	0.005	3.9e-05	0.34	Ls
E13	0.080	0.082	0.067	0.488	0.473	0.036	3.5e-05	0.39	Sl
E14	0.096	0.061	0.055	0.498	0.530	0.084	7.9e-05	0.61	Sl
E15	0.175	0.057	0.047	0.394	0.476	0.038	4.9e-05	0.14	Sl
E17	0.344	0.049	0.079	0.494	0.461	0.072	2.89e-05	0.62	Sl
E18	0.204	0.042	0.045	0.397	0.531	0.146	7.8e-05	0.34	Sl
E19	0.031	0.060	0.117	0.456	0.515	0.116	8.4e-06	0.61	Sl

905

906 [1] GEPPA is a French soil texture classification. The texture labels correspond to SS: pure sand, Sl:
907 silty sand, Ls: sandy silt, LL: pure silt.

908

Table 3. Comparison between the CEC determined in the laboratory for the core samples and the CEC determined from the inverted field data using the petrophysical transforms described in the main text. We need to remember that the comparison is only qualitative for various reasons (i) the spatial support between the core sample (cm scale) and the field data (m scale) is not the same and (ii) the CEC of the laboratory data include the CEC of humic substances (which does not impact the SIP data). For the clay core sample, the CEC is taken from Table 4 (direct measurement with the cobalt hexamine method) while the field CEC is the average of the CEC of the tomogram for the clay formation from the geophysical field data.

Sample	Measured CEC (meq/100g)	Field CEC (meq/100g)	Texture GEPPA
E1	11.9	7.6	SS
E2	9.5	7.7	SS
E3	7.2	13.7	Sl
E4	16.1	10.7	SS
E5	16.6	10.5	Ls
E6	15.5	12.2	Ls
E7	7.8	13.0	LL
E8	7.2	13.1	Ls
E9	11.5	6.2	SS
E10, E11	7.7	8.2	Sl
E12	20	15	Ls
E13	15.8	12.1	Sl
E14	19.9	12.1	Sl
E15	9.8	15.6	Sl
E17	17.9	10.2	Sl
E18	12.3	12.6	Sl
E19	11.5	13.5	Sl
Clay	40.2	43±12	AA

Table 4. Physical properties of a clay core sample drilled in the vicinity of the test site in the same clay formation.

Property	Clay end-member
CEC (meq/100g)	40.2
Soil type (GEPPA)	AA
Depth of extraction (m)	2.1-2.2
Clay (vol.%)	67.1
Silt (vol.%)	6.6
Sand (vol.%)	26.3

Figures

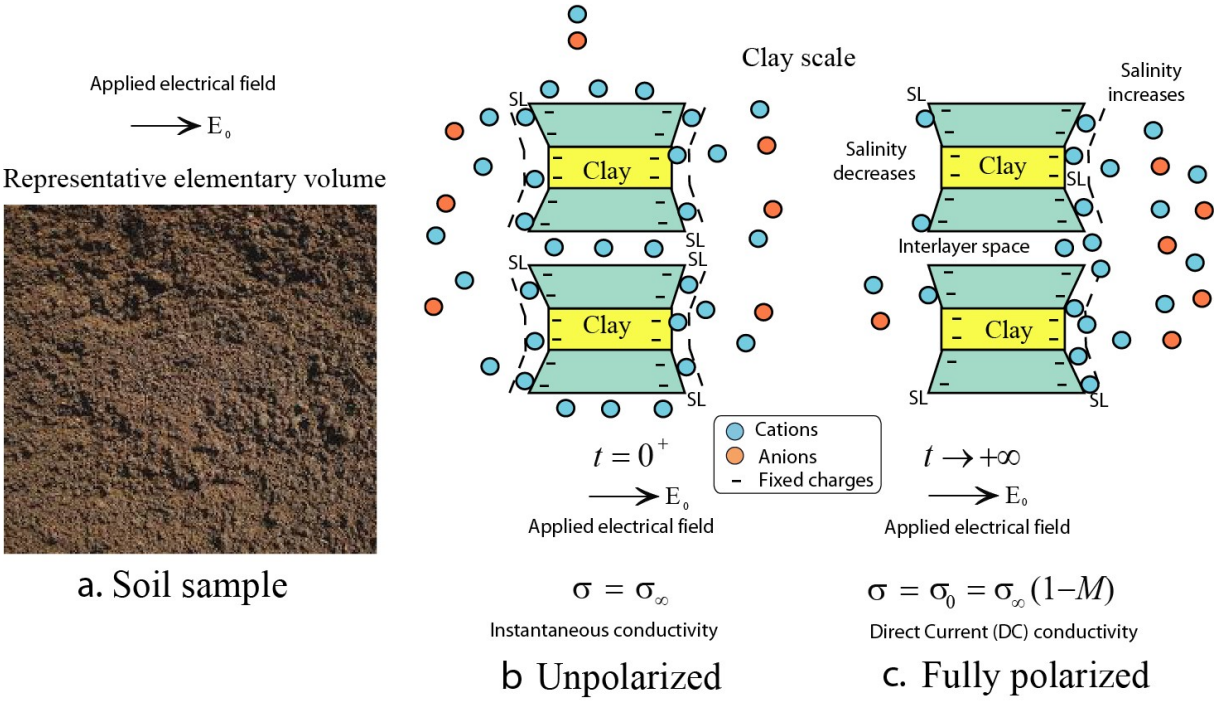

Figure 1. Polarization of the clay particles due to an applied (external) electrical field $\mathbf{E}_0$. **a.** Soil sample submitted to an applied electrical field $\mathbf{E}_0$. **b.** At the particle scale, the grains are surrounded by an electrical double layer (e.g., Gouy, 1910; Stern 1924). When the external electrical field is applied, the charge carriers are all mobile. They all participate to the surface (interfacial) conduction process (at t=0+ just after the shut down of the primary current). The instantaneous conductivity σ_∞ corresponds to this state. **c.** When the external electrical field has been applied for a long time, the clay particle gets fully polarized. The ionic charge carriers associated with the polarization of the clay do not contribute to the conduction process anymore. In this situation, the conductivity of the material corresponds to the Direct Current (DC) conductivity σ_0, which is necessarily smaller than the instantaneous conductivity. SL stands for the Stern Layer. M (dimensionless) denotes the chargeability.

938

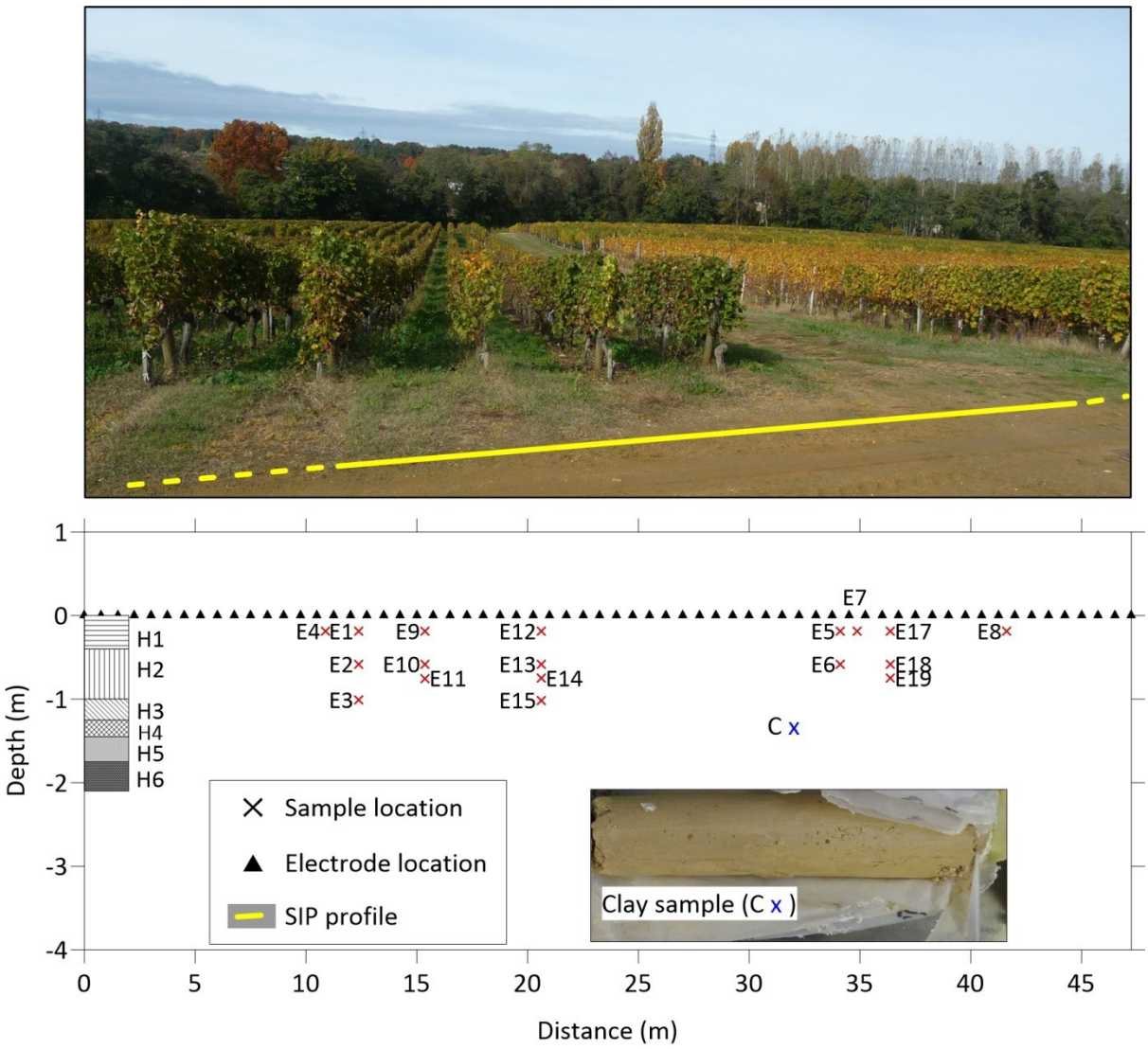

939

940

941 **Figure 2.** Description of the test site. Upper panel: Image showing the position of the
942 geophysical profile in the vineyard. Lower panel: Six soil horizons (H1-H6) have been
943 defined at the site. Soil samples (labeled E1 to E19) used for the petrophysical interpretation
944 were extracted along the profile from Horizons H1 and H2. SIP stands for Spectral Induced
945 Polarization.
946

947

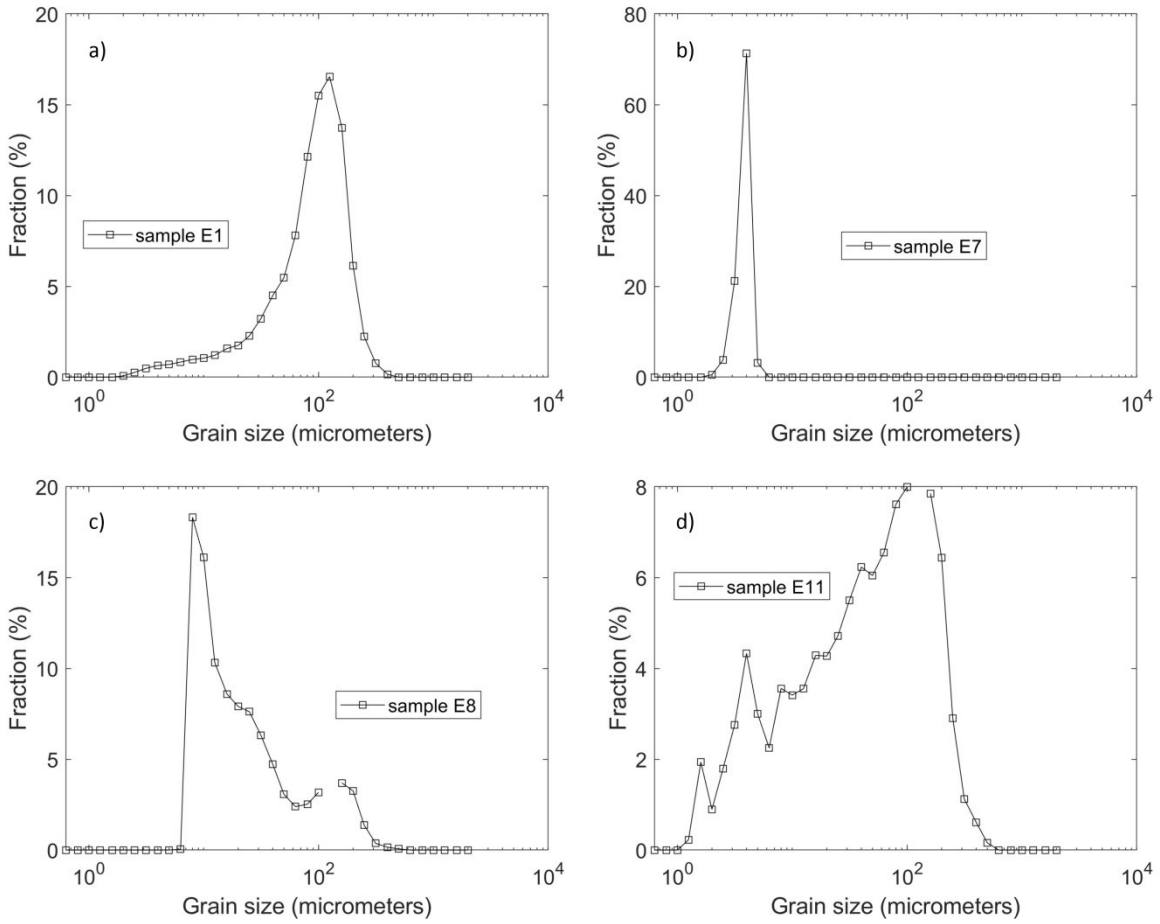

948

949

950 **Figure 3.** Grain size distribution of some selected core samples. **a.** Sample E1. **b.** Sample E7.
951 **c.** Sample E8. **d.** Sample E11. The broadness of the grain size distribution can be very
952 different between the different samples. The c-exponent of sample E7 is 0.39 consistent with
953 the narrow grain size distribution exhibited by this core sample. The c_1-exponent of sample
954 E11 is 0.30 consistent with a broad grain size distribution.
955

956

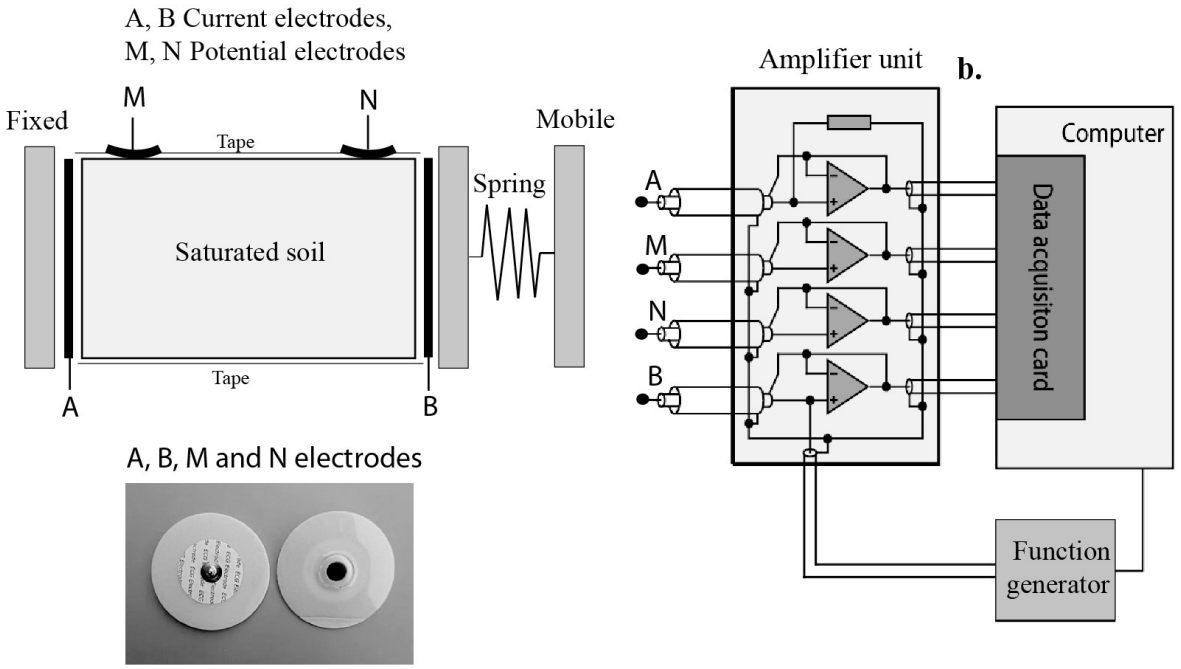

957 **a.** Complex conductivity cell **b.** ZEL-SIP04-V02 impedance meter
958

959

960 **Figure 4.** Spectral induced polarization measurements of a soil. **a.** Conductivity cell with the
961 electrodes. **b.** ZEL-SIP04-V02 impedance meter operating in the frequency range 1 mHz-45
962 kHz (Zimmerman et al., 2008). The precision in phase measurement of this instrument is ~0.1
963 mrad below 1 kHz. A test of the sample holder can be found in Revil et al. (2018a).
964
965

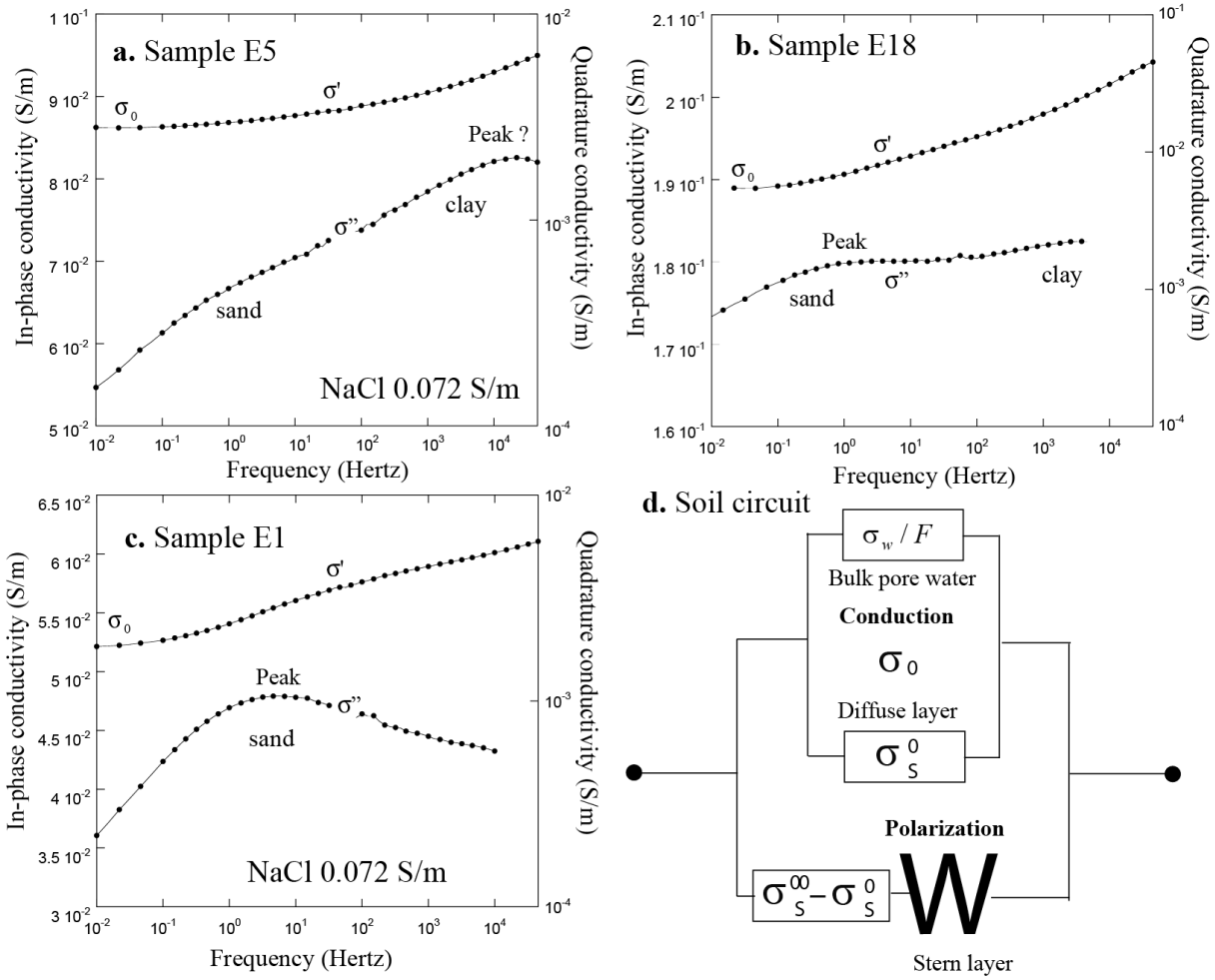

966

967

968 **Figure 5.** In-phase (σ') and quadrature conductivity (σ'') spectra of a soil. **a.** Sample E5. **b.**
969 Sample E18. **c.** Sample E1. **d.** Equivalent electrical circuit for a soil corresponding to equation
970 (4), where W denotes a Warburg-type capacitance corresponding to the polarization of the
971 Stern layer (the inner component of the electrical double layer). The conduction process
972 through a soil sample comprises two contributions: A bulk conductivity in the liquid pore
973 water and a surface conductivity associated with the electrical double layer. The quantities σ_S^{∞}
974 and σ_S^{0} represent the instantaneous and DC surface conductivity, respectively. The relaxation
975 time is associated with the polarization length scales (pore sizes or grain sizes) of the soil. The
976 data with a standard deviation higher than 5% have been removed.
977

978

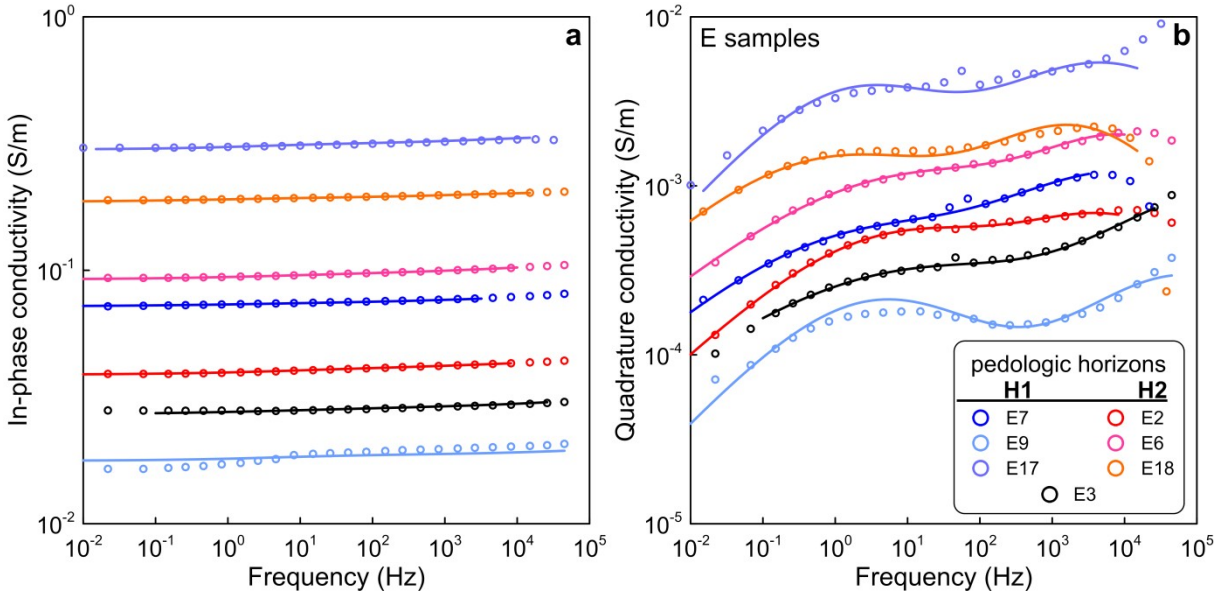

979

980

981 **Figure 6.** Selected examples of 7 complex conductivity spectra (in-phase and quadrature
982 conductivity) fitted with the double Cole Cole model described in Appendix A (plain lines, 6
983 core samples shown here). **a.** In-phase conductivity spectra. **b.** Quadrature conductivity
984 spectra. We have not used the high and low-frequency data with an RMS error >10%./ High
985 frequency errors are generally due to electromagnetic coupling effects while low frequency
986 errors are generally due to stability issues with the electrodes.
987

988

989

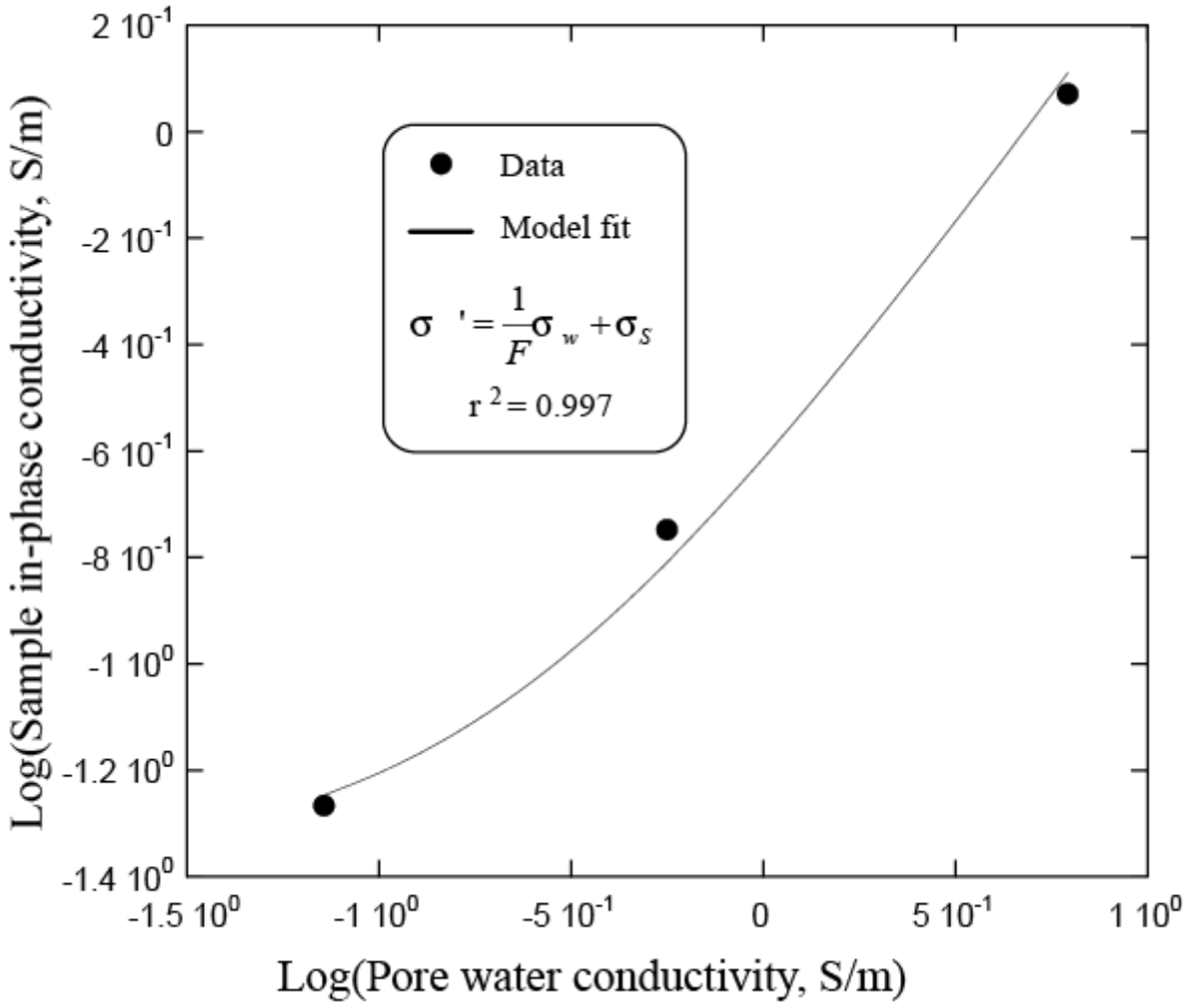

Figure 7. Determination of the formation factor F and surface conductivity σ_S using the in-phase conductivity of the core sample σ' (at 1 Hertz) versus the pore water conductivity σ_w. The fit of the conductivity model is done in a log-log plot to ensure the surface conductivity is correctly estimated. The formation factor and the surface conductivity are estimated for each sample (the formation factor as the slope of the trend). The fit is done by a non-linear least square regression technique in a log log space (see Revil et al., 2017a). The formation factor and surface conductivity values are reported in Table 1. Note that surface conductivity depends on the frequency but this dependence is small (less than 10%) owing the value of the chargeability M_1.

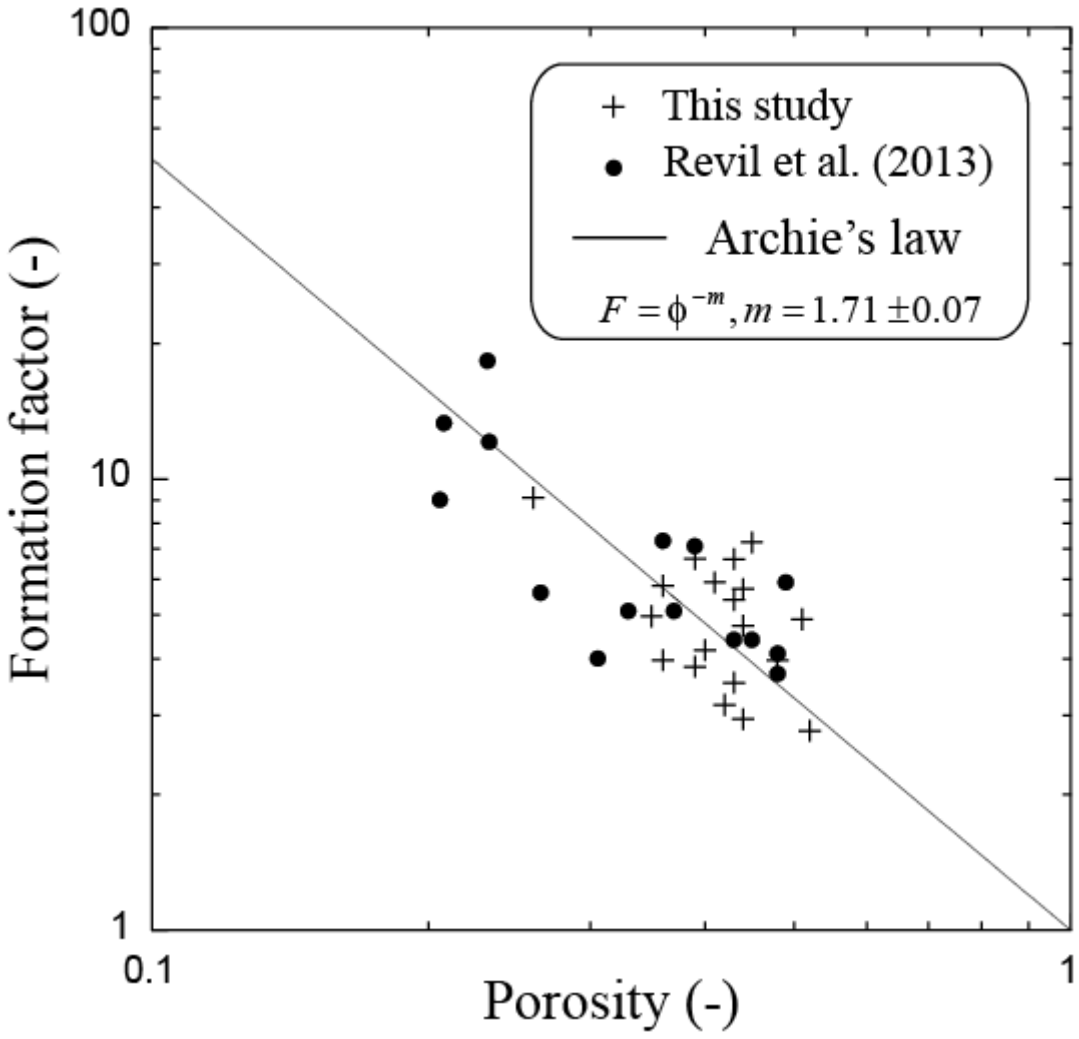

Figure 8. Fit of Archie's law between the formation factor F and the (connected) porosity ϕ for this study and the Revil et al. (2013) study on saprolitic soils to increase the data base on the low-porosity side. The best power-law regression (r^2 = 0.87) is used to obtain an average value of the cementation (porosity) exponent m using all the core samples. Using only the laboratory data from Table 1, we obtain m = 1.78 ± 0.35 (r^2 = 0.58)*:*

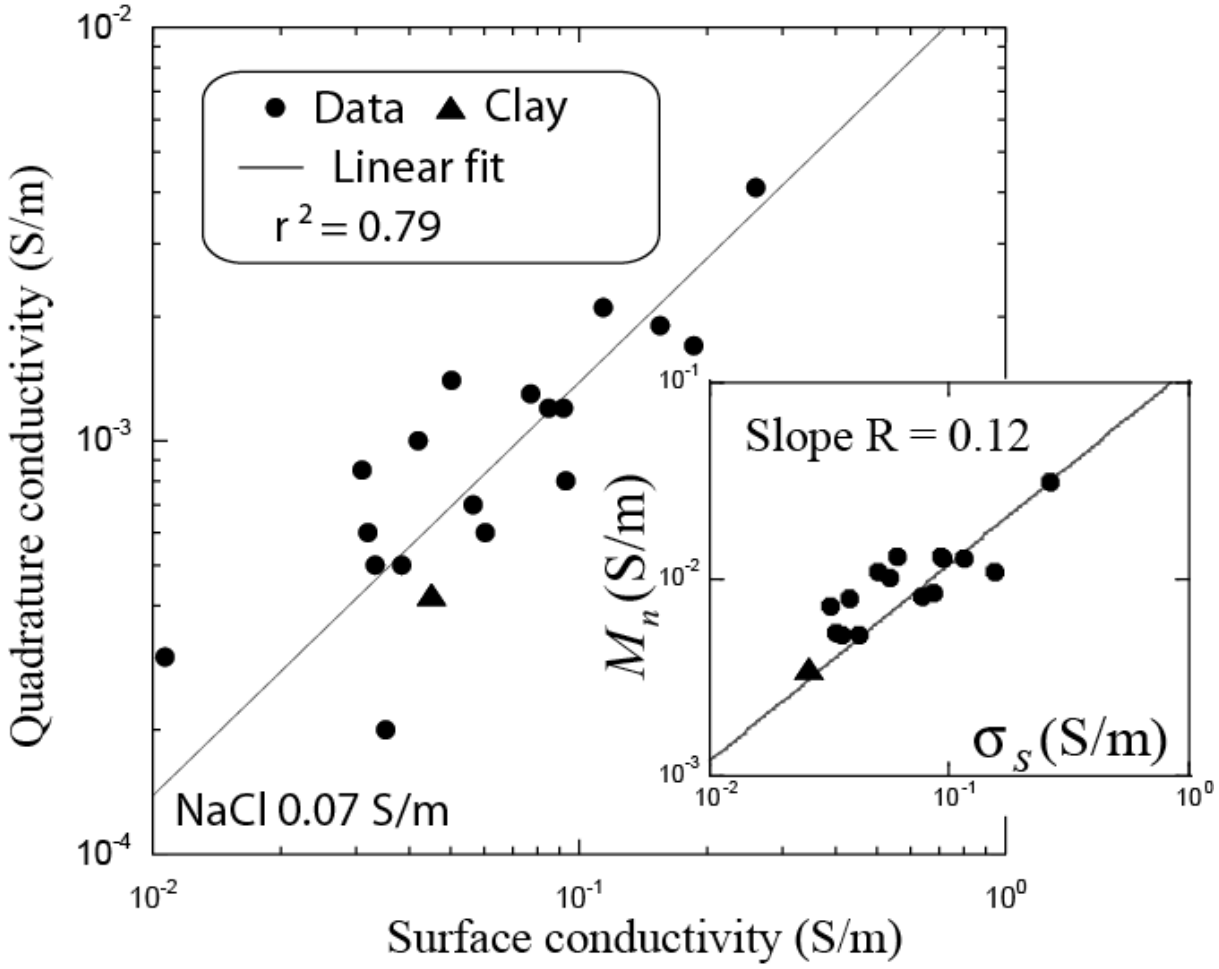

Figure 9. Quadrature versus surface conductivity (1 Hertz). For the soil samples we obtain – σ''/σ_S = 0.0140±0.001. Using $R = -\alpha\sigma''/\sigma_S$ and α = 8.8 (from equation 11, 6 orders of magnitude), we obtain R = 0.12. According to the dynamic Stern layer model, this trend is independent of the value of the formation factor and the porosity of the core samples. This confirms the results of Weller et al. (2013). Insert: Normalized chargeability M_n versus surface conductivity σ_S. The normalized chargeability is given from Table 2 as $M_n = (M_1+M_2)/\sigma_s$. The slope yields the following value for the dimensionless factor R = 0.12. The filled triangle corresponds to the clay pole investigated only through the field measurements assuming that the conductivity of the core sample is dominated by its surface conductivity component.

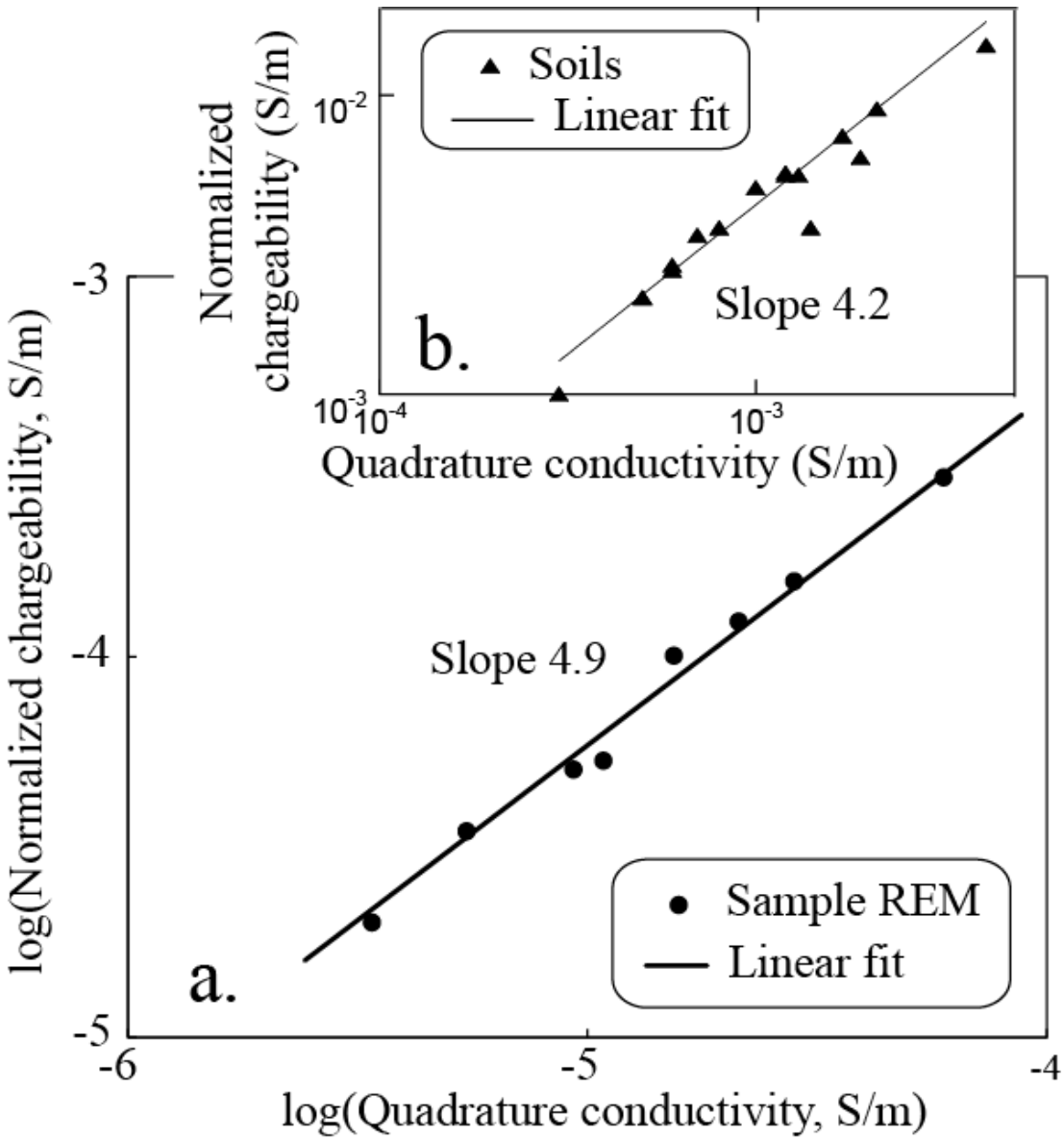

Figure 10. Relationship between the normalized chargeability (between the frequencies 1 Hertz and 1 kHz) and the quadrature conductivity at the geometric frequency of 32 Hertz. Different water saturations. **a.** REM Samples at different saturations. **b.** Soil samples at full water saturation. The slope α is found to be 4.9 for the REM samples (soil samples used as Ram Earth Material, REM, regression coefficient $r^2 = 0.97$) and 4.2 for the soils while the theory (equations 8 and 9, $r^2 = 0.92$) predicts a slope of 4.4. If the normalized chargeability would be determined over 6 orders of magnitude, we would expect to have $\alpha = 8.8$.

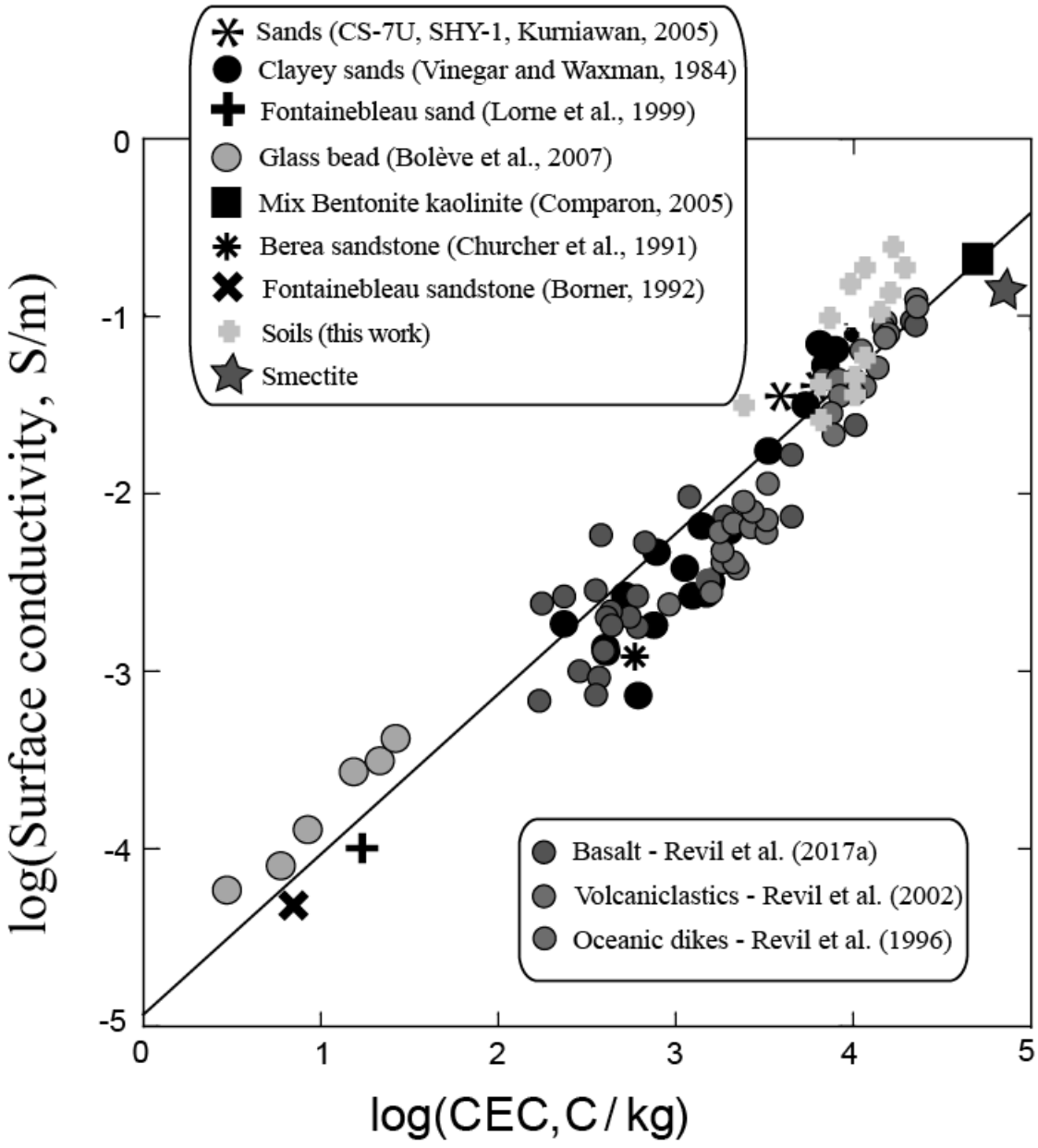

Figure 11. Surface conductivity versus cation exchange capacity (CEC) for high porosity (>0.20, saturated) core samples. The data from the literature are from Bolève et al. (2007, glass beads, NaCl), Vinegar and Waxman (1984, shaly sands, NaCl), Churcher et al. (1991) (CEC for the Berea sandstone), Lorne et al. (1999, Fontainebleau sand KCl), Kurniawan (2005, clean sand, Sample CS-7U), Börner (1992, sample F3 Fontainebleau sandstone), and Comparon (2005, mixtures of MX80 bentonite and kaolinite). The volcanic rock data are from Revil et al. (1996) and Revil et al. (2002). The overall trend confirms the linear dependence (r^2 = 0.94 in a log–log space) between the surface conductivity and the CEC for high porosity core samples.

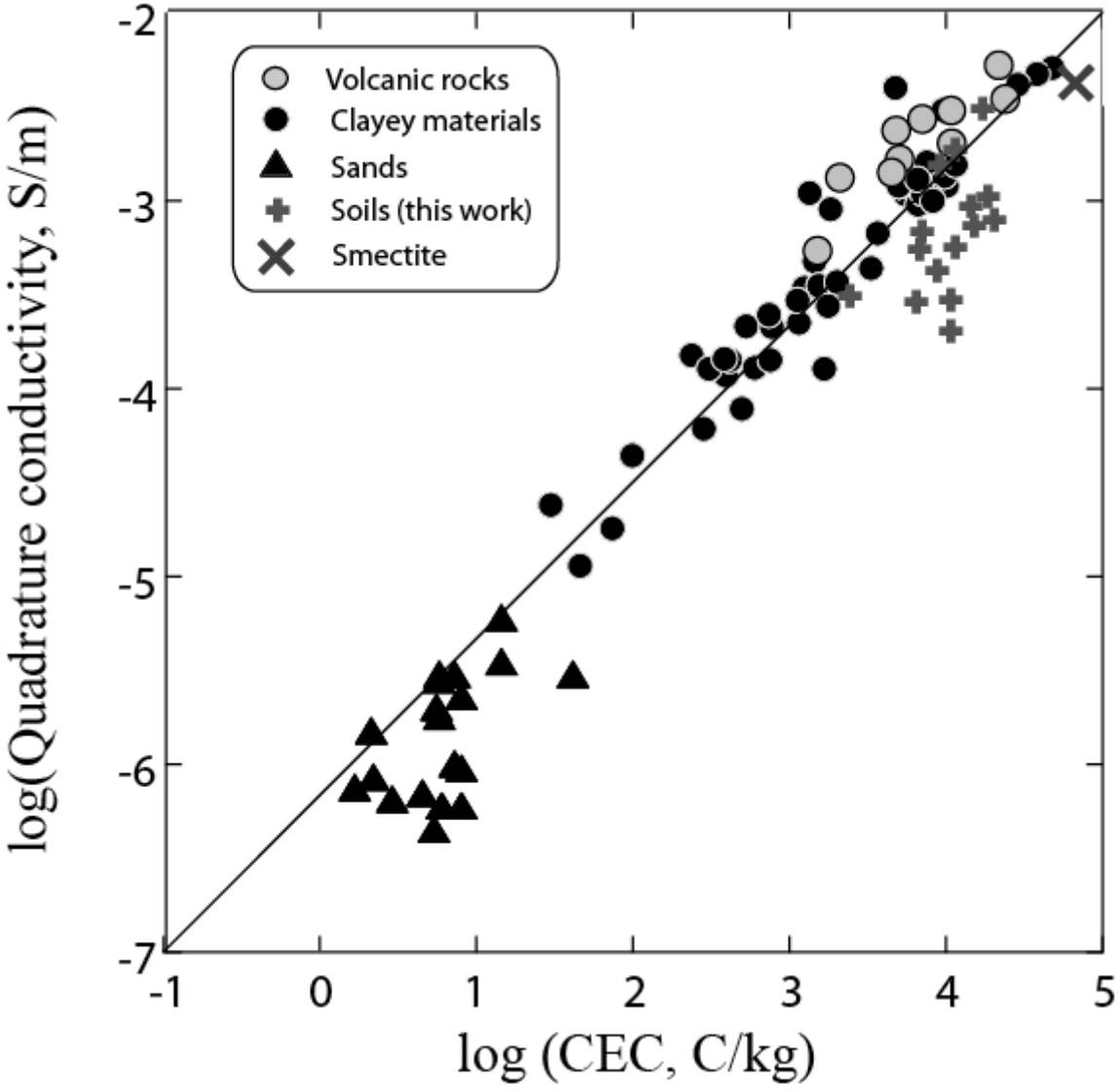

Figure 12. Quadrature conductivity (1 Hertz) versus cation exchange capacity (CEC, cobalthexamine method) for high porosity (>0.20, saturated) core samples. The data shown in the figure are Revil et al. (2017a, b, c) and Revil et al. (2018a). The overall trend confirms the linear dependence (r^2 = 0.91 in a log–log space) between the quadrature conductivity and the CEC for high porosity core samples. Note: 1 meq /(100 g) = 963.2 C kg^{-1}.

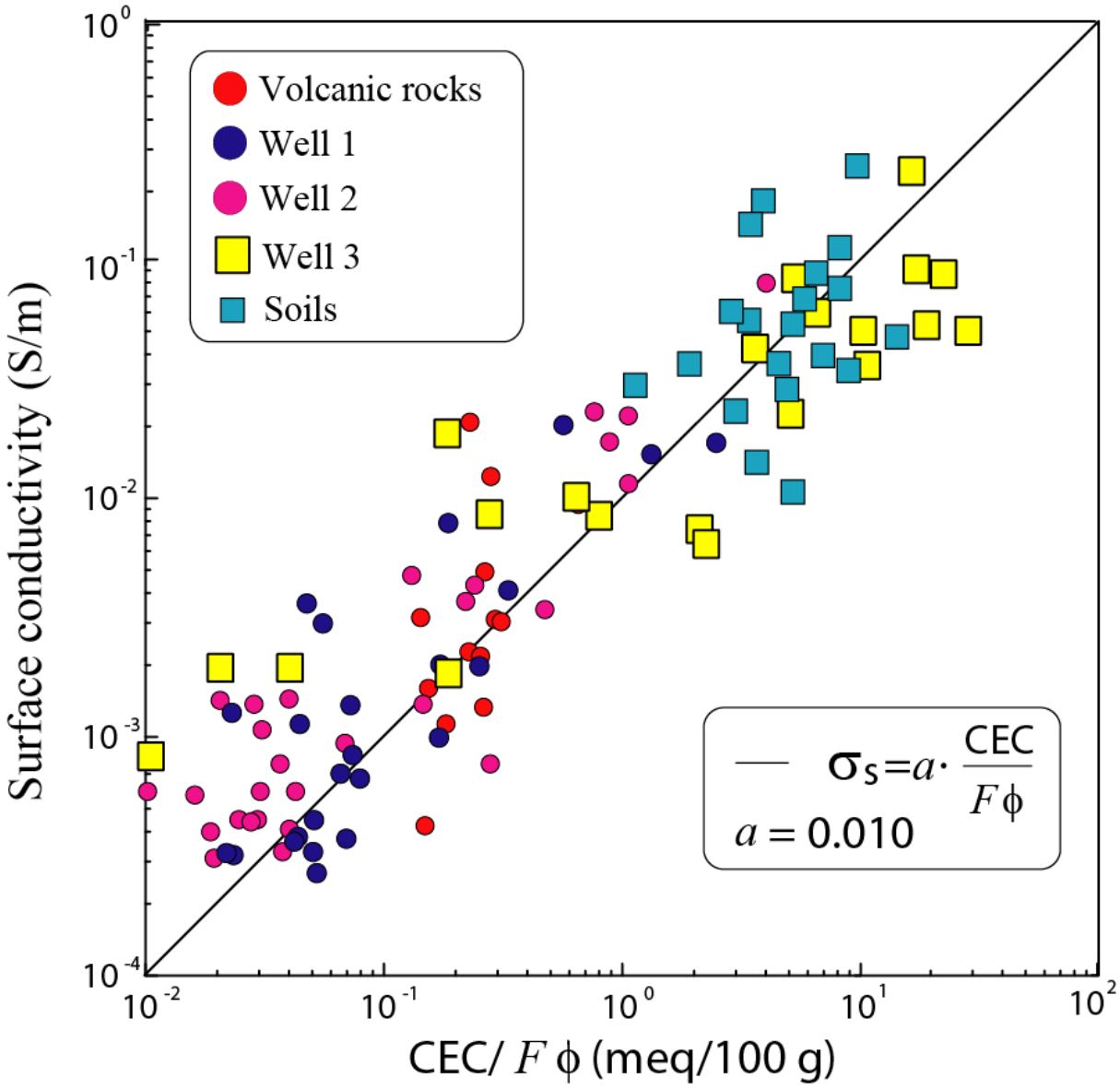

Figure 13. Surface conductivity versus normalized cation exchange capacity (CEC divided by the tortuosity, which is given by the product of the formation factor F by the porosity ϕ) for samples characterized by a broad range of porosity. The slope a is consistent with the theory presented in the main text for which $a = \rho_g B = 8.2\times10^{-6}$ kg $s^{-1}V^{-1}$= 0.008 S m^{-1} /(meq/100 g) close to the best fit value (0.010 S m^{-1} /(meq/100 g)). Note that here we are using siliciclastic materials, which explain the value of ρ_g. For carbonate-rich soils, the mass density of the grains is higher (ρ_g= 2800 kg m^{-3}). Data from Revil et al. (2021, volcanic rocks).

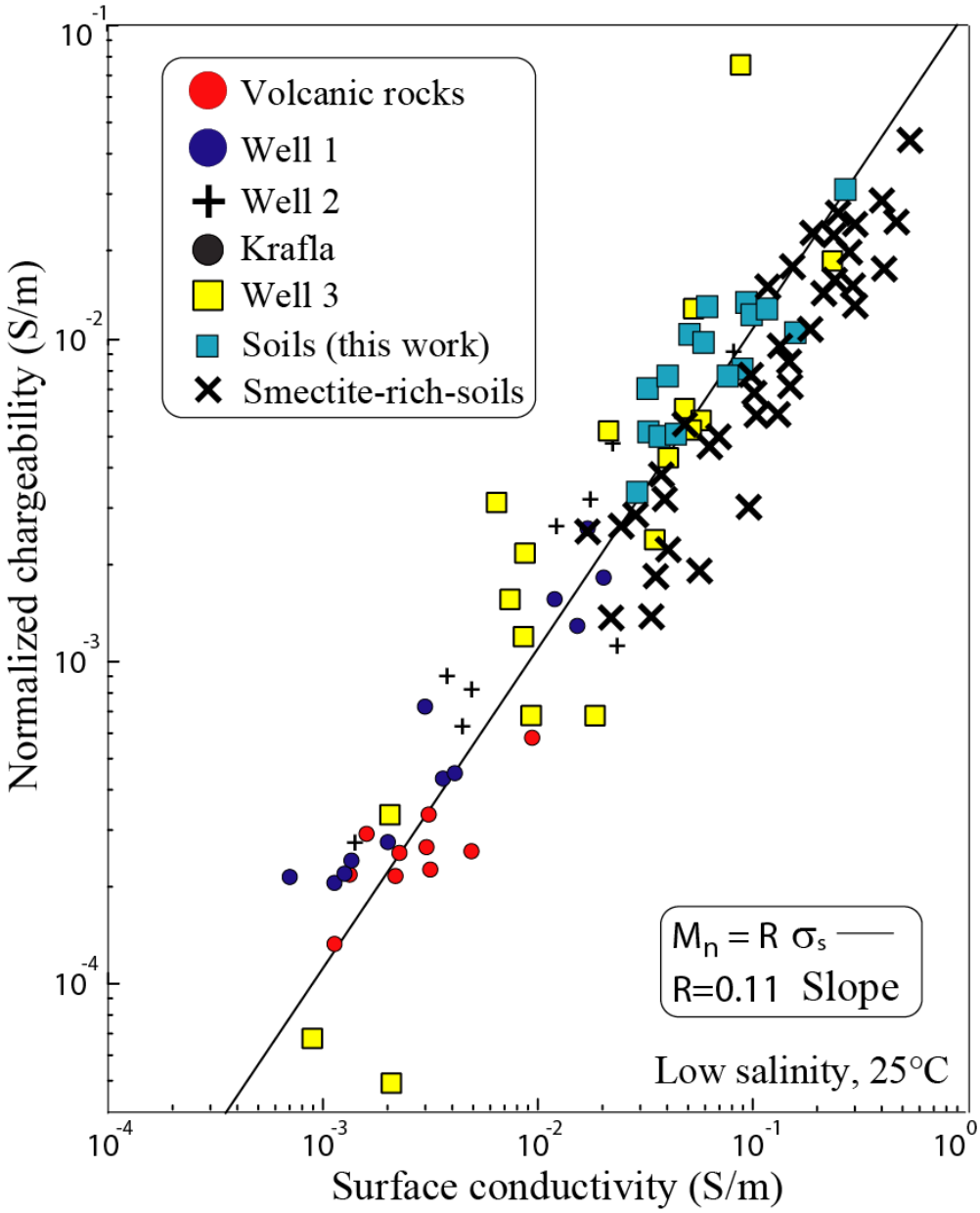

Figure 14. relationship between normalized chargeability and surface conductivity. Comparison between the soil samples of the present study, the smectite-rich soil samples from the study of Revil et al. (2017a) and volcanic rock samples (consolidated and not consolidated) from Hawaii and Krafla volcanoes (in Iceland, see Revil et al., 2018 and Ghorbani et al., 2018) excluding core samples with magnetite or pyrite. The slope of the trend provides the value of the funadamental dimensionless coefficient R, which is consistent with previous estimates of this parameter. Data from Revil et al. (2021, volcanic rocks) and Revil et al. (2017a, smectite-rich soils).

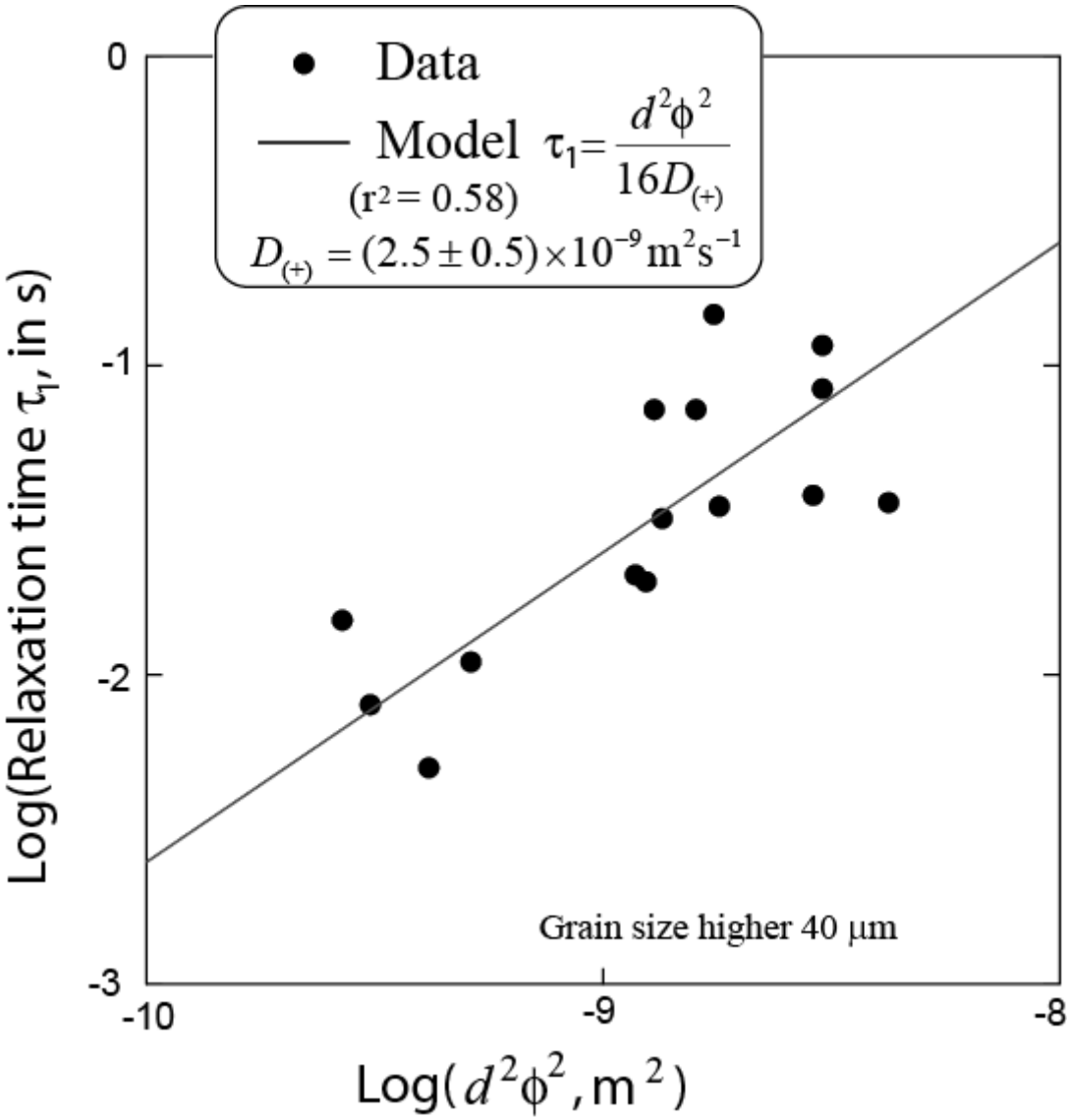

Figure 15. Relaxation time versus grain size (mean of the distribution above 40 μm) times the porosity for the sandy materials of the present study (saturated core samples). We use the relaxation time τ_1 corresponding to the coarse fraction of the material (see Table 2). The linear trend (r^2 = 0.58 in a log-log space) is used to compute the value of the diffusion coefficient $D_{(+)}$ = (2.5±0.5)×10^{-9} m^{2}s^{-1}. Only the sandy cores (grain size higher than 40 μm have been considered here).

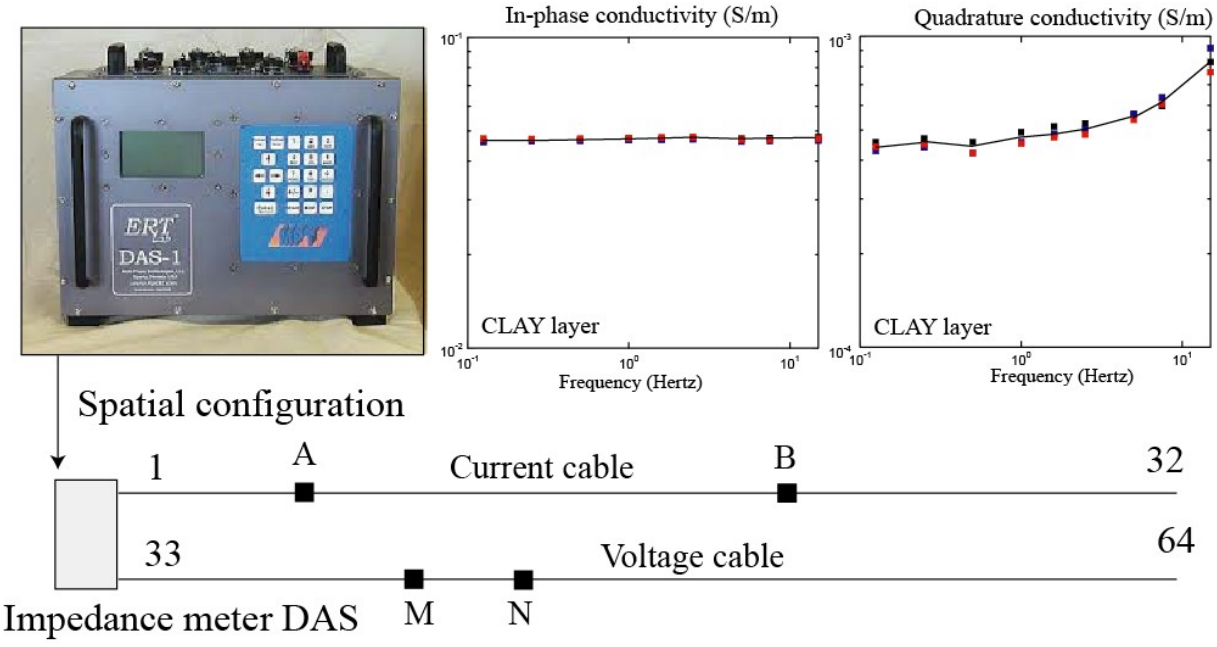

Figure 16. Setup of the field acquisition system. The current electrodes AB and the voltage electrodes MN are locates along separated cables to limit capacitive and inductive coupling effects. The acquisition was done with a Wenner-type configuration with a total of 64 electrodes. We use an impedance meter operating in the frequency-domain (DAS-1 from Multi-Phase Technologies, LLC). The figure displays also the complex conductivity spectra obtained in the field from this equipement at three locations corresponding to the clay layer.

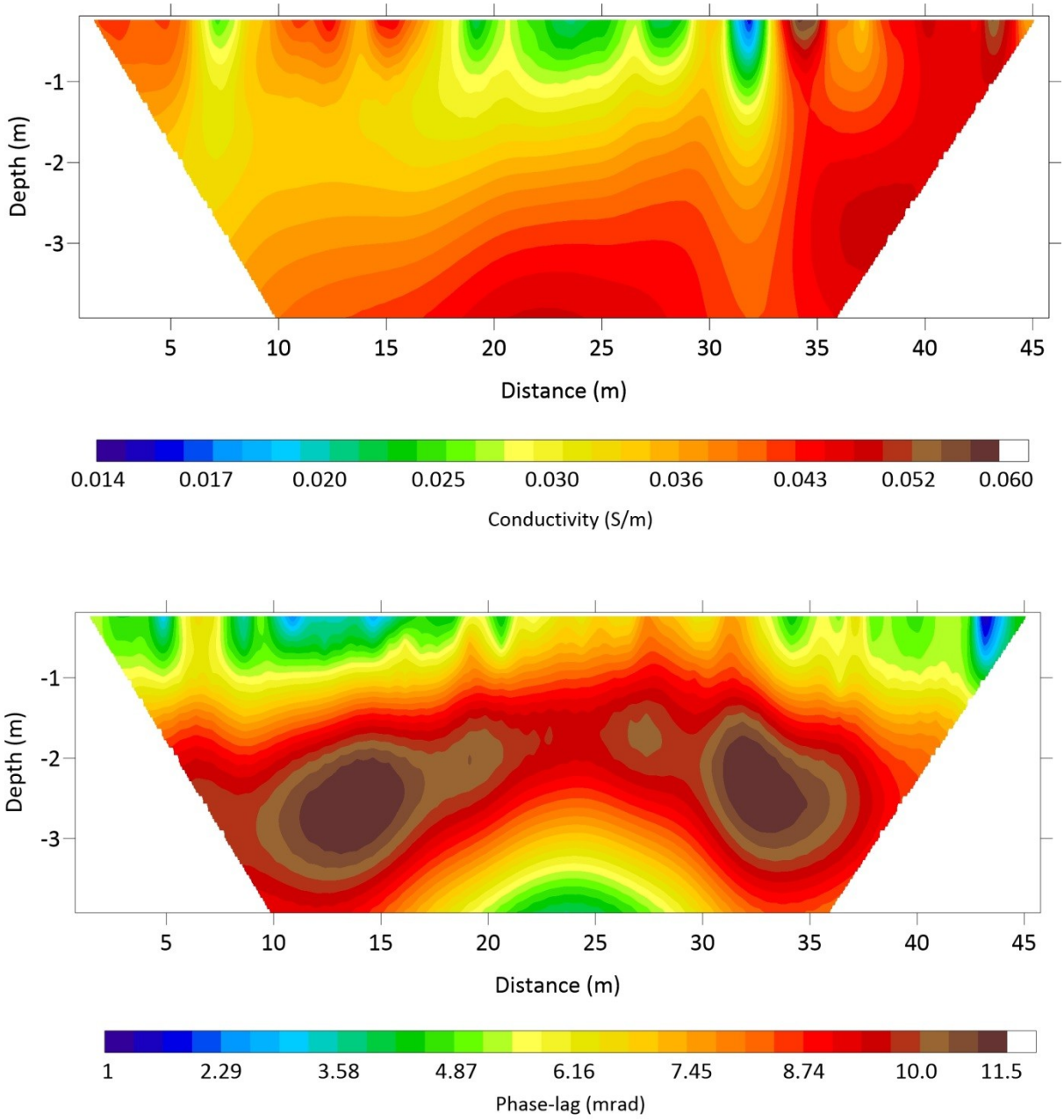

Figure 17. Conductivity and phase lag tomography for the geophysical profile shown in Figure 2 at 1 Hertz for the first 4 m below the ground surface. The conductivity profile does not display a lot of information while the phase exhibits a layer of high phase values (>9 mrad), possibly associated with a clay layer that has been recognized by drilling nearby.

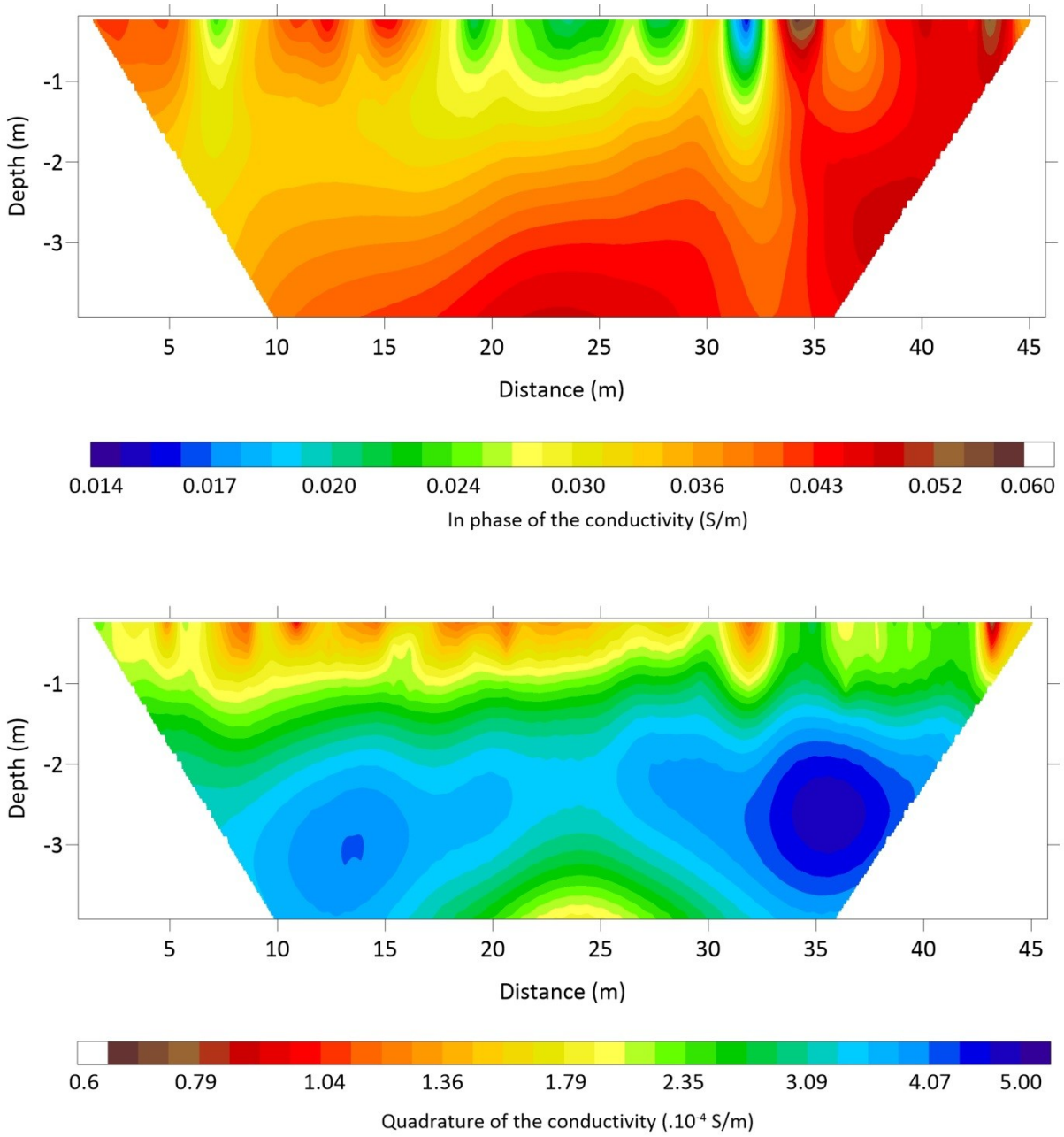

Figure 18. In phase and quadrature conductivity tomography for the geophysical profile P1 at 1 Hertz. The in-phase conductivity does not show clear structures while the quadrature conductivity tomogram displays a folded layer characterized by high values of the quadrature conductivity (> 3×10^{-4} S m^{-1}).

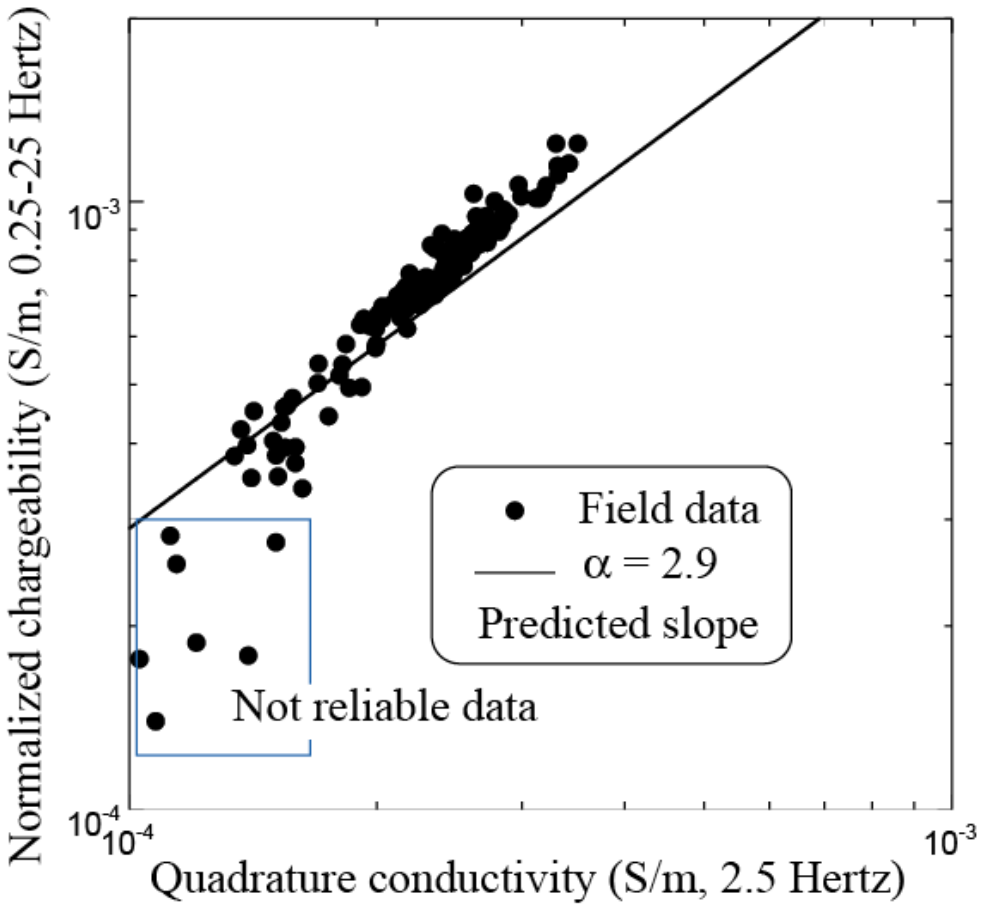

Figure 19. Normalized chargeability versus quadrature conductivity. The high and low frequencies (0.25 Hertz and 25 Hertz) are separated by 2 orders of magnitude, which yields a value of the slope equal to $\alpha = 2.9$ (from equation 9). Therefore the field data fairly agree with the model prediction (plain line) corresponding to equations (8) and (9). Please note that the plain line is therefore not a fit of the data in this plot. Low values in the quadrature conductivity are not reliable (see the outliers contained in the blue box).

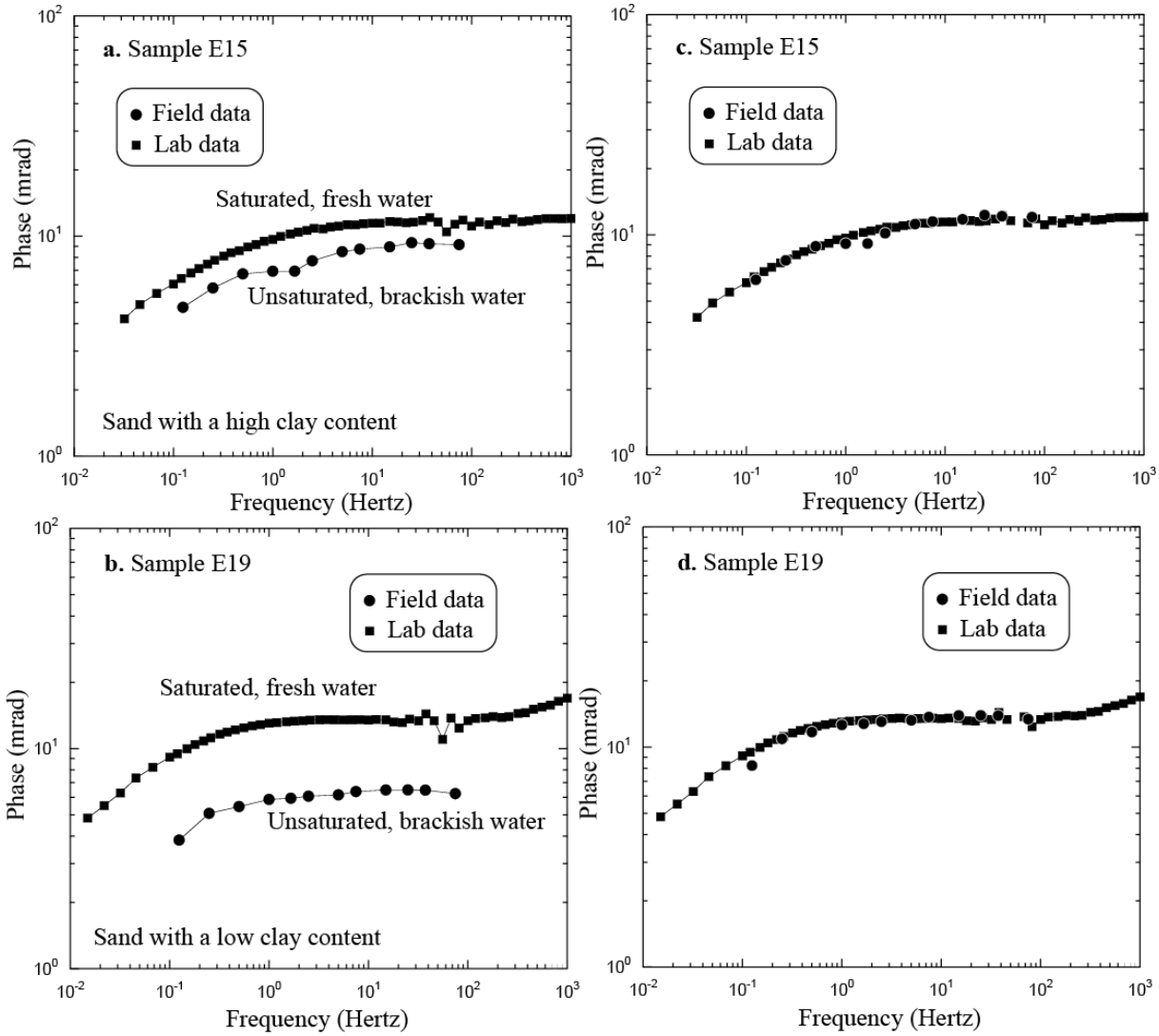

Figure 20. Comparison between the field and laboratory data. The field data are taken from the inverted tomograms at the position where the samples were extracted. The field data correspond to unsaturated conditions while the experimental data are taken at full saturation. **a.** Sample E15. **b.** Sample E19. **c.** Sample E15. Comparison of the phase spectra at saturation. **d.** Sample E19. Comparison of the phase spectra at saturation.

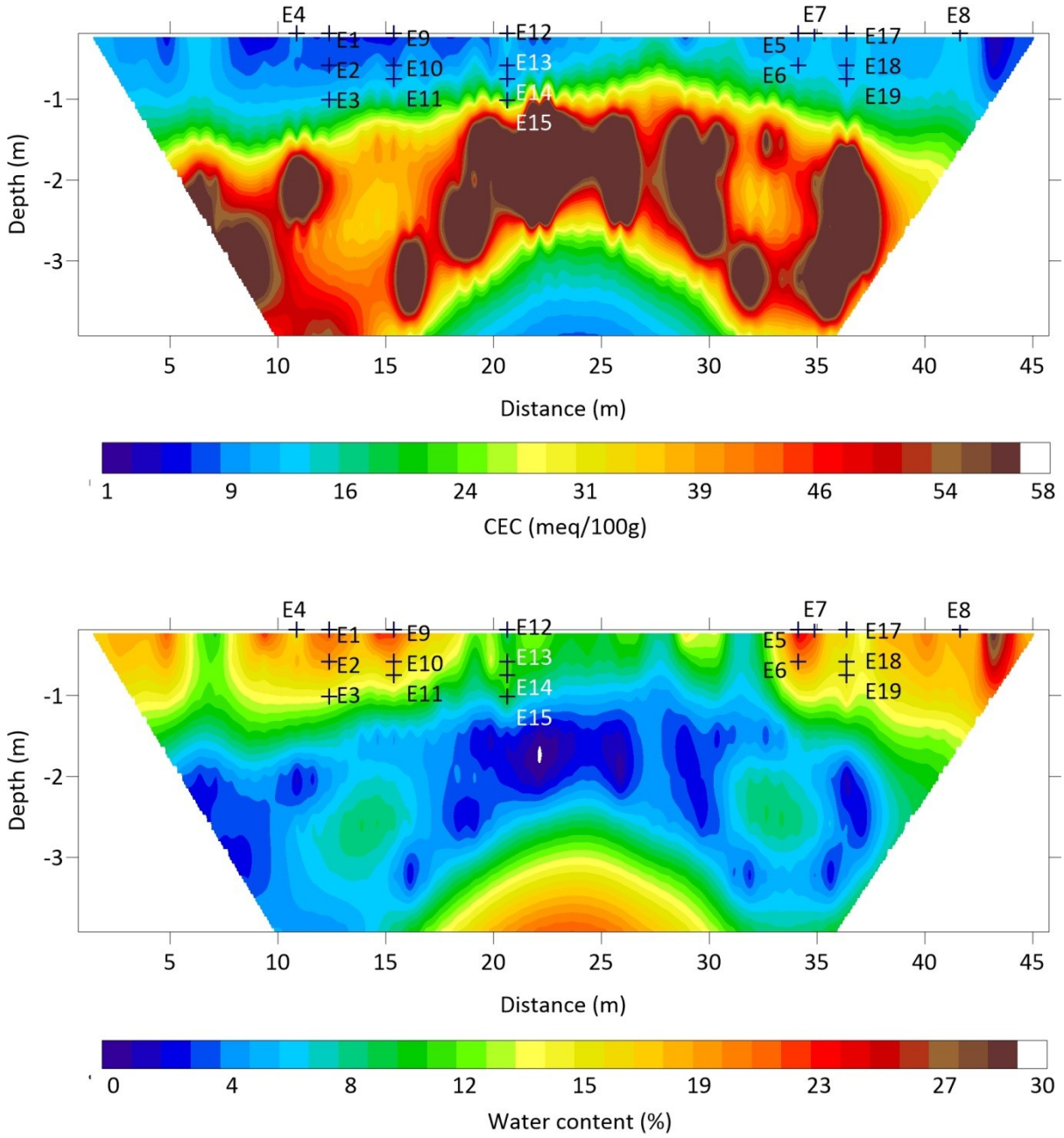

Figure 21. Tomography of the cation exchange capacity (CEC) and water content, θ, from the induced polarization tomography. From the tomogram, we observe a high-CEC low-water content dipping middle layer. Note that we use m = 1.7 for the full dataset but the true value of m in the clay formation is likely higher due to a higher CEC (see Revil et al., 1998, for an empirical trend between m and the CEC and the insert in Figure 14). A comparison between the CEC from the tomogram at the position of the core samples and the experimental data is given in Table 3.

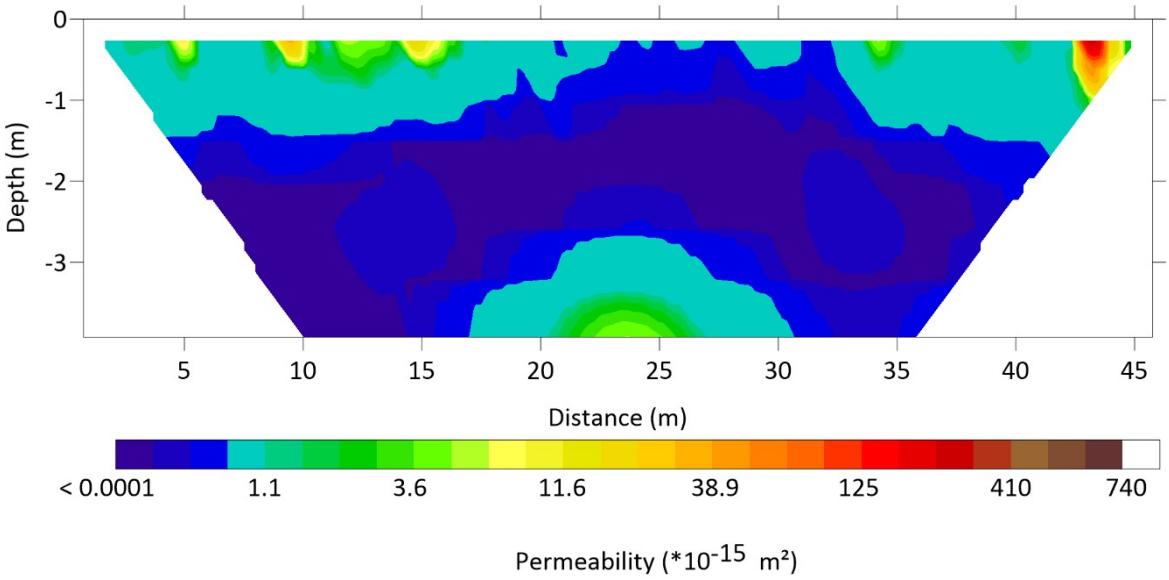

Figure 22. Soil permeability estimated from the data and spectral induced polarization tomography-based water content and cation exchange capacity (CEC) estimates. The estimation reveals that the middle layer is characterized by permeability values below 1 mD while the shallower (sandy) soils reach a permeability of 700 mD.

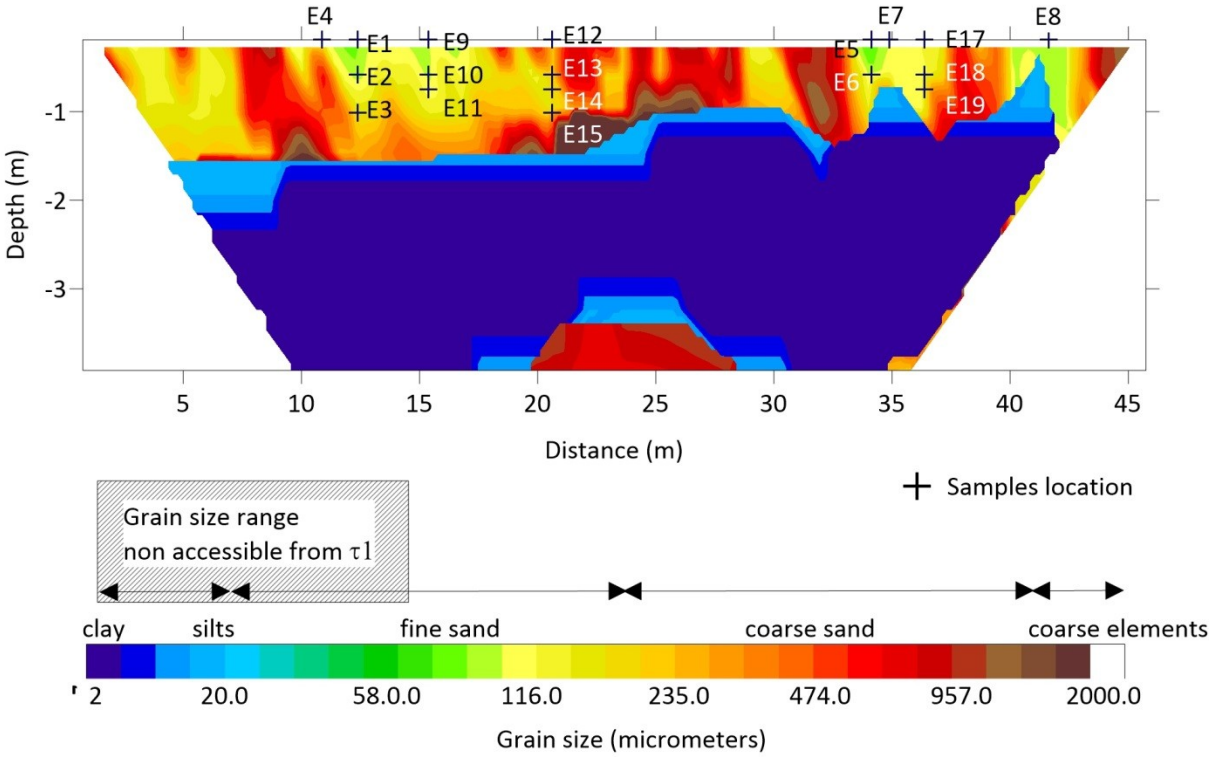

Figure 23. Tomography of the mean grain size from the relaxation time distribution determined from the spectra for each cell of the tomogram using a Cole Cole fit and the spectral induced polarization tomography-based water content values.

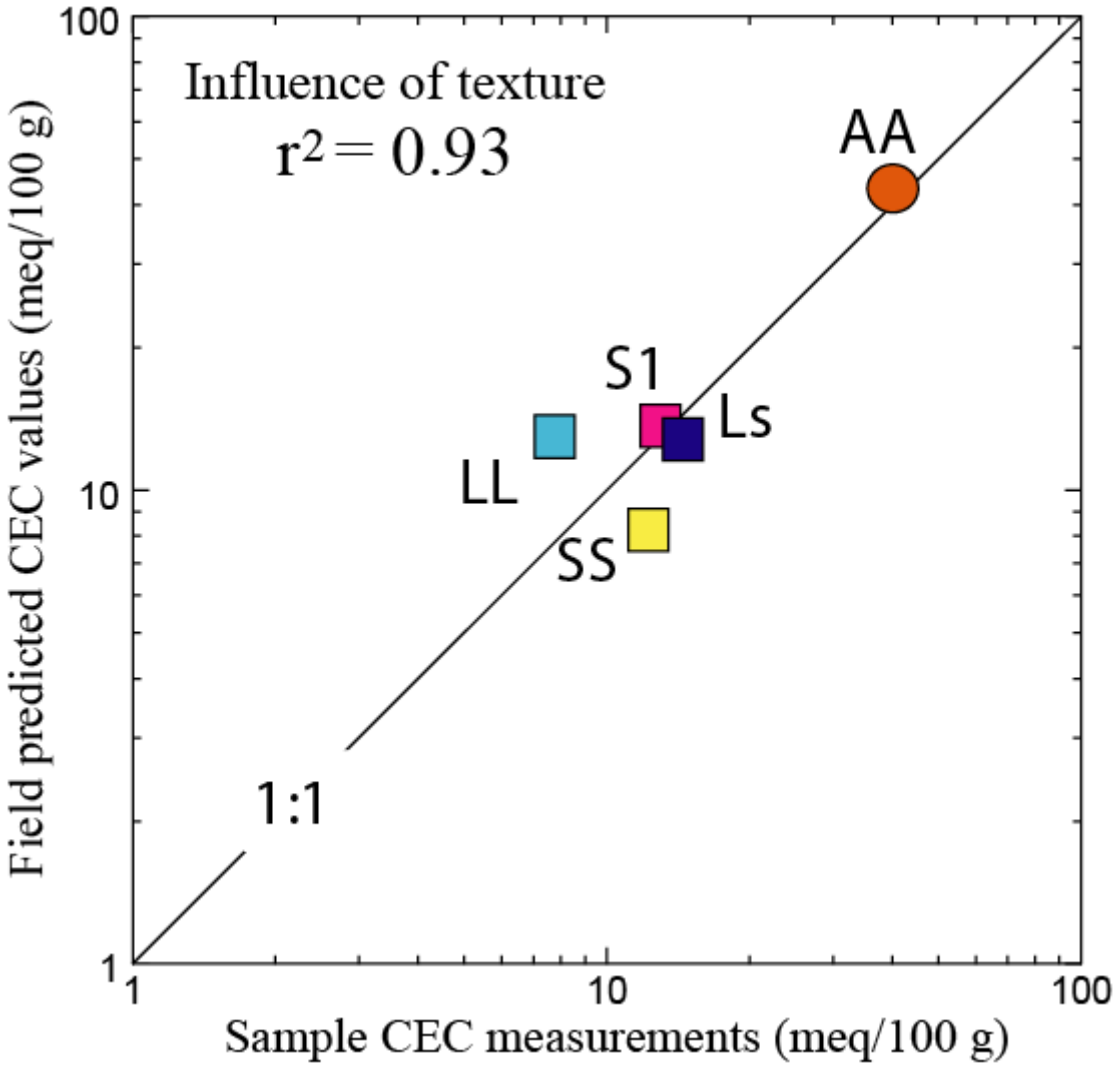

Figure 24. Field versus laboratory determination of the cation exchange capacity (in meq/100 g). The support volume of the laboratory core sample measurements is two orders of magnitude smaller than the support volume of the geophysical measurements. Therefore, we use here averaged values per texture type (SS: pure sand, Sl: silty sand, Ls: sandy silt, LL: pure silt, AA: clay end-member) for both the field and laboratory data to account for this point. The slope of the best least-square regression of a fit through (0,0) is 1.03. Forcing the fit to go through (0,0) is dictated by the underlying physics of the problem. The regression coefficient is given in a linear space.

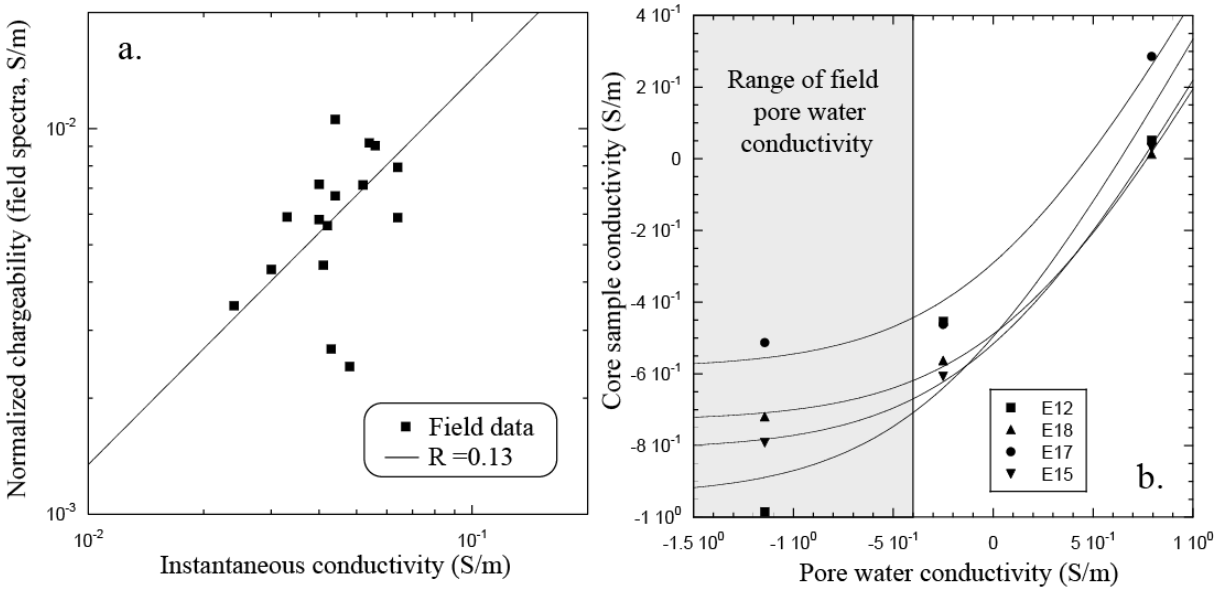

Figure 25. Importance of surface conductivity for the brine-saturated core samples. **a.** Normalized chargeability versus instantaneous conductivity (field data at the position of the core sample). The value of the slope indicates that surface conductivity dominates the conductivity response of the soils. **b.** Conductivity of the core sample versus the pore water conductivity in a log-log plot. In grey, we have plotted the range of the field pore water conductivity from fresh to brakish. For the full range, the data indicates that surface conductivity dominates the conductivity response of the material. R is indeed a constant independent of the relative importance of surface conduction. This is not the value of R that indicates if the surface conductivity dominates but the ratio between the normalized chargeability and the conductivity. This ratio is close to R if and only if surface conduction dominates.